

A Computationally Tractable Scheme for Simulation of the Human Pulmonary System

Brody H. Foy*, David Kay

Department of Computer Science, University of Oxford, Wolfson Building, Parks Road, OX1 3QD, Oxford, UK

Abstract

The accurate analysis of patient lung structure and morphology in a clinical setting is one of the significant challenges in pulmonary medicine. In recent years, computational modelling techniques have been shown to help improve understanding of function-form relationships within the lungs, and of the underlying sensitivities of pulmonary function test responses to pulmonary disease. A large array of literature has been dedicated to modelling airflow and gas transfer within the lungs, and within vasculature. However, little work exists connecting the two systems together, particularly in computationally tractable ways. Within this study we outline a numerical scheme for modelling gas transport throughout the airways, pulmonary arterial network, and across the alveolar-capillary membrane. Through careful scheme design, and the application of high-performance computing structures, we show how these models can remain tractable, even when simulating to quite fine resolution. Following model development and error analysis, we apply the model to the simulation of the multiple-breath washout, a common pulmonary function test, illustrating how the choice of tracer gas may affect clinical diagnosis measures.

Keywords: Pulmonary, washout, computational, lungs, blood flow

☆

*Corresponding author

Email address: `brody.foy@new.ox.ac.uk` (Brody H. Foy)

1. Introduction

The lungs are an incredibly complex pair of organs, whose function is strongly driven by both shape and morphology. Due to this, one of the most significant challenges within pulmonary medicine is the accurate analysis of patient lung structure, and ventilation mechanics. In recent years, computational modelling approaches have been developed with the aim of better understanding the human pulmonary system, and its response to diseases.

A large array of modelling techniques have been developed [1, 2, 3, 4], often with the aim of improving understanding of pulmonary function test (PFT) responses to disease. Airway ventilation is typically simulated in either a 1D [2] or 3D-1D hybrid [5] environment, performed on virtual lungs created from histological data [6], or patient-based airway structures created from a combination CT image extraction, and algorithmic generation[1, 7]. As computational power has improved, models have increased in complexity, and been able to capture behaviours at finer resolution within the airways.

Alongside airways models, similar modelling techniques have been applied to the bloodstream, and pulmonary arterial network [8, 9, 10]. Most commonly blood flow and artery cross-sectional area profiles are simulated using the Navier-Stokes equations in a 1D setting [11], or using a hybrid 3D-1D approach [12]. Similar to ventilation models, blood flow models are typically simulated upon histological-based[13, 14] or imaging based [15] virtual vasculature structures.

While there has been a large degree of work in both modelling pulmonary flow, and modelling ventilation, there is substantially less work which connects airflow and blood flow models together, to achieve full pulmonary simulation. Detailed models of alveolar-capillary gas exchange have been derived in the literature [4], however they have typically only been applied as compartmental models, limiting many potential avenues for analysis. This in part is driven by the significant computational constraint of building a full pulmonary model. Recent work by Kang et al. [16], has outlined a way to connect mechanistic models of the pulmonary arterial network and the airways, to achieve more holistic gas transport simulation. However, this model was presented with no significant analysis of computational tractability, and thus questions remain about its feasibility for widespread implementation.

Within this study, we address the literature gap by outlining an effective and tractable model of gas transport within the conducting zone of the lungs, the pulmonary arterial network, and across the alveolar-capillary mem-

brane. This model is primarily mechanistic, allowing for realistic simulation of blood flow, air flow, and gas transfer between the two networks. By embedding these simulations in high-performance computing architectures, we show how simulation of the human pulmonary system can be both detailed and computationally tractable. We then illustrate the potential value of such a model, by applying it to the analysis of how the choice of tracer gas may affect outputs from the multiple-breath washout, a pulmonary function test experiencing increased clinical uptake.

2. Creation of a virtual lung and arterial structure

To build a detailed model for simulation of the pulmonary system, we first need a physically realistic virtual representation of the lungs and pulmonary arterial network. Within this study simulations of the pulmonary system were performed using a set of 26 patient-based 1D structures (8 healthy subjects, 18 asthmatic subjects), taken from a set originally presented by Bordas et al. [1]. Structures were created through a combination of CT segmentation (to generation 6-10), and algorithmic airway generation within the identified lobar boundaries (to an average generation 16) [17]. Each airway tree consisted of between 30-100,000 branches, 15-50,000 of which were terminal bronchioles; each of which was subtended by a spherical acinar unit.

Construction of the arterial network was performed through modification of the patient-specific airway tree. We assume that the pulmonary arteries mimic the airway structure, with identical branching angles and ratios [6], but with resting radii (the radii at standard pressure) reduced by 75%, to match healthy histological data [18]. At the distal ends of the left and right main bronchi this similarity to the airway tree ends, and subsequently we artificially create the left and right pulmonary artery, by extending a centreline directly away from the mid-point where the two inferior pulmonary arteries meet. Instead of creating an artificial pulmonary trunk, the artery network is left as two distinct structures, for the left and right lung respectively.

The veins in the network were assumed to be symmetric to the arteries, with each terminal artery connected to the associated terminal vein by a single capillary branch, with equal radius to the artery. This is illustrated in a schematic diagram in Figure 1. The capillaries were assumed to wrap around each acinar region, covering approximately 1/5 of their surface area

73 (a justification of this is given in Appendix A), leading to a capillary length

$$l_{\text{cap}} = \frac{2\pi R_{\text{acin}}^2}{5R_{\text{cap}}^0}, \quad (1)$$

74 where R_{acin} and R_{cap}^0 are the radius of the acinar region and capillary respec-
 75 tively. It should be noted that given the acinar regions expand and contract
 76 over time, the length of each capillary also fluctuates in response.

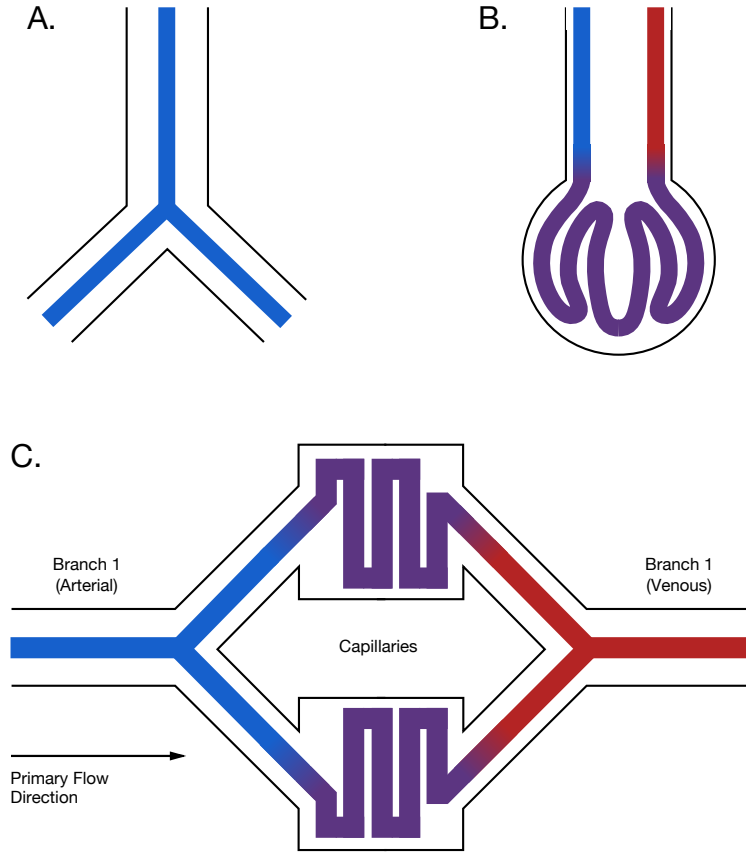


Figure 1: **Diagram of the arterial network.** A cross-section of the arteries against the airways can be seen (A), as well as a 2D representation of the capillaries wrapping around the acini (B). An unravelled 2D schematic of the symmetry between artery and vein networks is also given (C).

77 We note that the construction of the arterial network is based on signifi-
 78 cant simplifying assumptions about branch lengths and radii. However, the
 79 modelling techniques outlined in this study do not rely on the specific nature
 80 of the structure, and would be suitable for application to any appropriately
 81 formatted 1D representation of the lungs and associated arterial pulmonary
 82 network.

83 3. Pulmonary model

84 To effectively simulate gas transport throughout the pulmonary system,
 85 five different models are needed: for ventilation, blood flow, gas transport in
 86 the airways, gas transport in the bloodstream, and gas transfer across the
 87 alveolar-capillary membrane. Within this section we detail each model and
 88 its numerical implementation.

89 3.1. Ventilation model

Detailed explanations of the ventilation and airways gas transfer models have appeared in the prior work of Foy et al. [2, 19, 20]. In brief, the flow rate Q within each airway is assumed to be driven by the pressure gradient ΔP over the branch. Each terminal bronchiole is subtended by a spherical acinar region V_{acin} , whose expansion and contraction is proportional to the terminal bronchiole flow rate, and constrained by local tissue compliance \mathbb{C} , and the pressure difference from the acinus to the pleural cavity. This is expressed by the equation system

$$\Delta P = R(Q)Q, \quad \text{for each branch,} \quad (2)$$

$$Q_{\text{upper}} = \sum Q_{\text{lower}}, \quad \text{for each bifurcation,} \quad (3)$$

$$\frac{d}{dt}V_{\text{acin}} = Q, \quad \text{for each terminal branch,} \quad (4)$$

$$P_T - P_{pl}(t) = \frac{1}{\mathbb{C}}V_{\text{acin}}, \quad \text{for each terminal branch.} \quad (5)$$

90 where $R(Q)$ is Poiseuille branch resistance, with a modification for energy
 91 dissipation [21], P_T is the pressure at the distal end of the terminal branch,
 92 and P_{pl} is the pleural pressure. A diagram of the ventilation domain is given
 93 in Figure 2.

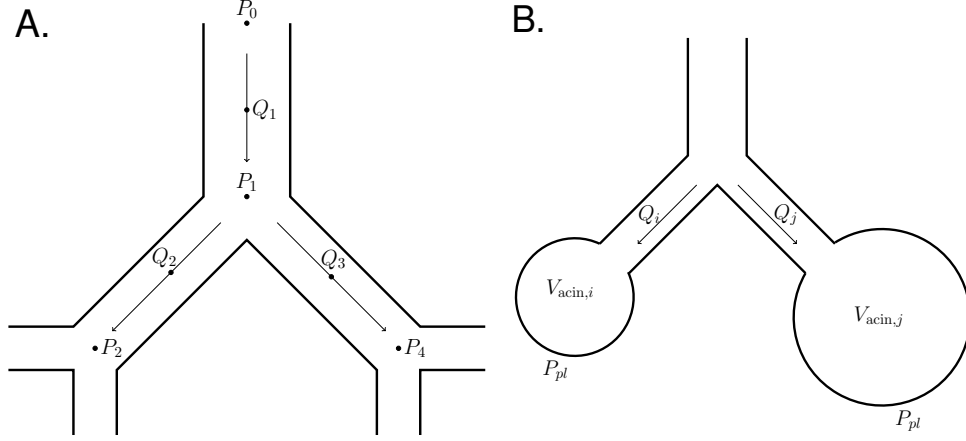


Figure 2: **Diagram of the ventilation model domain.** An idealised 2D cross-section of the model domain, showing branch bifurcations, flow rates and pressures (A), and the connection of terminal bronchioles to acinar regions (B).

The pleural pressure is chosen to enforce the desired breathing pattern and frequency (typically sinusoidal for tidal breathing), with a linear gravitational gradient on its range (see Foy et al. [2] for more details).

System (2)-(5) was implemented numerically using a Backward Euler discretisation for the temporal derivative, leading to a system of the form

$$\mathbf{F}(\mathbf{x}) = \mathbf{0},$$

at each time step, where \mathbf{x} is the collection of pressure, flow and volume variables. This system is solved using vector Newton iterations, of the form

$$\mathbf{x} = \mathbf{x} - \mathcal{J}^{-1}\mathbf{F}(\mathbf{x}),$$

until $\|\mathbf{F}(\mathbf{x})\|_2$ falls below a desired tolerance.

As the majority of the Jacobian (\mathcal{J}) is constant, it can be efficiently formed directly, and inverted using an LU factorisation following approximate-minimum-degree reordering.

3.2. Airways gas transport model

In the absence of bloodstream interactions, the ventilation model outlined above is used to drive a gas transport model in the airways, first proposed

108 by Paiva [22]:

$$\frac{\partial C}{\partial t} = D \frac{\partial^2 C}{\partial x^2} + \frac{D}{A} \frac{\partial A}{\partial x} \frac{\partial C}{\partial x} - u \frac{\partial C}{\partial x}, \quad (6)$$

109 where $C(x, t)$ is the gas concentration at position x and time t , A the airway
 110 cross-sectional area, $u = Q/A$ the air velocity, and D the diffusion coefficient
 111 for the gas in air.

112 To implement this model numerically, we first discretise the domain into a
 113 series of N nodes, with corresponding concentration values C_i ($i = 1, \dots, N$).
 114 Multiple nodes are placed on each branch, a single node is placed at the centre
 115 of each acinar region, and a single node is placed slightly proximal to each
 116 bifurcation, as illustrated in Figure 3.

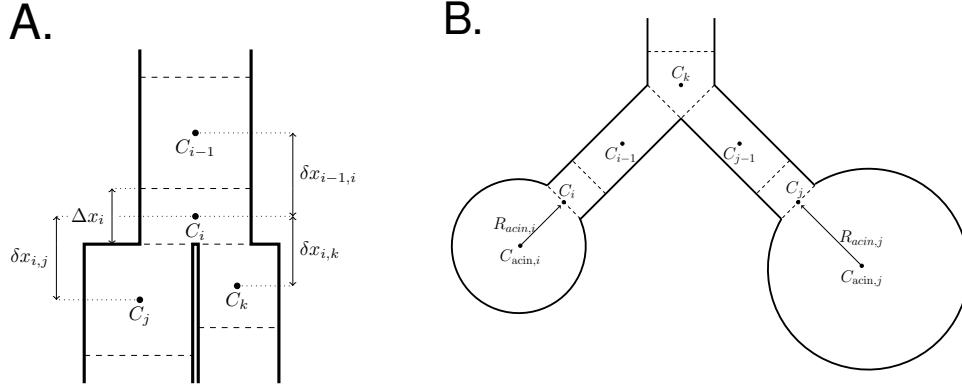


Figure 3: **Diagram of the airways gas transport model domain.** An idealised cross-section of the model domain, showing concentration nodes and finite difference boundaries in the branches (A), and the acinar regions (B).

The gas transport model is then implemented numerically using a finite difference scheme, originally outlined by Dutrieue et al. [23]. For each node

at a bifurcation, and considering the notation in Figure 3, we have

$$\begin{aligned}
\frac{dC_i}{dt} = & \frac{D}{\Delta x_i} \left(\frac{1}{A_j + A_k} \left\{ \frac{[C_j - C_i]A_j}{\delta x_{i,j}} + \frac{[C_k - C_i]A_k}{\delta x_{i,k}} \right\} - \frac{C_i - C_{i-1}}{\delta x_{i-1,i}} \right) \\
& + \frac{D}{2A_i} \left(\frac{\left\{ A_j - A_i \frac{A_j}{A_j + A_k} \right\} [C_j - C_i]}{\delta x_{i,j}^2} + \frac{\left\{ A_k - A_i \frac{A_k}{A_j + A_k} \right\} [C_k - C_i]}{\delta x_{i,k}^2} \right) \\
& + \begin{cases} \frac{u_i C_i - u_{i-1} C_{i-1}}{\Delta x_i}, & \text{during inspiration} \\ \frac{u_j C_j + u_k C_k - u_i C_i}{\Delta x_i}, & \text{during expiration.} \end{cases} \quad (7)
\end{aligned}$$

117 A similar formula can be derived for nodes within a branch, by treating it as
 118 a single branch bifurcation, and setting appropriate terms to zero.

119 At the tracheal boundary, the system is convection-dominated meaning

$$\frac{\partial C}{\partial \mathbf{n}} = \begin{cases} u_1 C_{\text{ext}}, & \text{during inspiration} \\ u_1 C_1, & \text{during expiration,} \end{cases}$$

120 where \mathbf{n} is the normal vector outwards from the boundary, and C_{ext} is the
 121 external gas concentration.

122 At each terminal bronchiole boundary gas transfer occurs between the
 123 acinus and the bronchiole. To account for this, we enforce the boundary
 124 condition

$$\frac{\partial C_i}{\partial \mathbf{n}} = D \frac{C_{\text{acin},j} - C_i}{R_{\text{acin},j}} - \begin{cases} u_i C_i, & u_i > 0 \\ u_i C_{\text{acin},j}, & u_i \leq 0. \end{cases}$$

125 where $R_{\text{acin},j}$ is the radius of the acinar region, calculated as

$$R_{\text{acin},j} = \left(\frac{3}{4\pi} V_{\text{acin},j} \right)^{1/3}.$$

126 Gas concentrations in each acinus fluctuate accordingly to the gas transfer

127 from the terminal bronchiole, and changes in acinar volume, meaning

$$\frac{dV_{\text{acin},j}C_{\text{acin},j}}{dt} = \begin{cases} Q_i C_i - DA_i(C_{\text{acin},j} - C_i)/R_{\text{acin},j}, & Q_i > 0, \\ -DA_i(C_{\text{acin},j} - C_i)/R_{\text{acin},j}, & Q_i \leq 0. \end{cases} \quad (8)$$

128 The total model for gas transport in the airways is solved using a combination
 129 of Euler methods and operator splitting. Firstly, all temporal derivatives in
 130 the airways are discretised using a Backward Euler method. This allows
 131 for airway gas concentrations to be updated through solution of a matrix
 132 problem

$$A\mathbf{C}^{n+1} = \mathbf{C}^n + \mathbf{f}(\mathbf{C}^n, \mathbf{C}_{\text{acin}}^n),$$

133 where A is a convection-diffusion matrix, \mathbf{C}^n and $\mathbf{C}_{\text{acin}}^n$ are the airway and
 134 acinus concentrations at time step n , and \mathbf{f} accounts for boundary conditions
 135 between terminal bronchioles and the associated acini. The matrix inversion
 136 is solved using a standard LU factorisation, after application of approximate-
 137 minimum-degree reordering.

138 Following the calculation of \mathbf{C}^{n+1} , the updated acinar concentrations
 139 ($\mathbf{C}_{\text{acin}}^{n+1}$) are calculated by applying a Forward Euler discretisation to Equation
 140 (8).

141 3.3. Blood flow model

142 To model blood flow, we build upon the work of Olufsen et al. [11].
 143 By considering experimental data, Olufsen [24] showed that there was an
 144 apparent function relationship between arterial wall thickness, vessel radius
 145 and vessel stiffness, such that

$$\frac{Eh}{R_b^0} = k_1 \exp(k_2 R_b^0) + k_3,$$

146 where k_1 , k_2 and k_3 are fitting constants, given in Table 1, and R_b^0 is the
 147 arterial radius under standard pressure.

148 Given this, we assume a linear stress-strain relationship between artery
 149 cross-sectional area (A_b), and pressure, such that

$$P_b = \frac{4}{3} \frac{Eh}{R_b^0} \left(1 - \sqrt{\frac{A_b^0}{A_b}} \right) = f(R_b^0) \left(1 - \sqrt{\frac{A_b^0}{A_b}} \right),$$

where A_b is the cross-sectional area of the vessel, and A_b^0 is the cross-sectional area at standard pressure. We combine this model with a 1D Navier Stokes equation, meaning

$$\frac{\partial A_b}{\partial t} + \frac{\partial Q_b}{\partial x} = 0, \quad (9)$$

$$\frac{\partial Q_b}{\partial t} + \frac{\partial}{\partial x} \left(\alpha \frac{Q_b^2}{A_b} + B \right) = -\frac{2\pi\nu_b Q_b R_b}{\delta A_b} + \frac{\partial B}{\partial R_b^0} \frac{dR_b^0}{dx}, \quad (10)$$

150 where Q_b is the flow rate, ν_b is the dynamic viscosity of blood, δ is the bound-
 151 ary layer thickness and ρ_b is the density of blood. The term $B = f\sqrt{A_b^0 A_b}/\rho_b$
 152 is an artificial term constructed to allow the equations to be written in con-
 153 servative form. The parameter α is a correction factor, presented by Sherwin
 154 et al. [25], which accounts for the shape of the uni-directional velocity pro-
 155 file. Within this study, for simplicity we take $\alpha = 1$, corresponding to a flat
 156 profile. In Appendix B, we compare flow profiles throughout the pulmonary
 157 system using $\alpha = 1.1$, showing strong concordance.

158 To simplify manipulations of equations (9)-(10), we introduce the nota-
 159 tion

$$\mathbf{U} = \begin{bmatrix} A_b \\ Q_b \end{bmatrix}, \mathbf{T} = \begin{bmatrix} \mathcal{T}_1 \\ \mathcal{T}_2 \end{bmatrix} = \begin{bmatrix} Q_b \\ \frac{Q_b^2}{A_b} + B \end{bmatrix}, \mathbf{S} = \begin{bmatrix} \mathcal{S}_1 \\ \mathcal{S}_2 \end{bmatrix} = \begin{bmatrix} 0 \\ -\frac{2\pi\nu_b Q_b R_b}{\delta A_b} + \frac{\partial B}{\partial R_b^0} \frac{\partial R_b^0}{\partial x} \end{bmatrix},$$

160 meaning the system can be written as

$$\frac{\partial}{\partial t} \mathbf{U} + \frac{\partial}{\partial x} \mathbf{T} = \mathbf{S}.$$

161 We solve this system numerically using a two-step Lax-Wendroff Method.
 162 First each arterial branch is discretise into M evenly spaced nodes (with
 163 spacing Δx), at N evenly spaced points in time (with time step Δt). We
 164 denote the value of U_b at node M , and time step n as U_M^n , and define inter-
 165 mediate step values as

$$\mathbf{U}_j^{n+1/2} = \frac{\mathbf{U}_{j+1/2}^n + \mathbf{U}_{j-1/2}^n}{2} + \frac{\Delta t}{2} \left(-\frac{\mathbf{T}_{j+1/2}^n - \mathbf{T}_{j-1/2}^n}{\Delta x} + \frac{\mathbf{S}_{j+1/2}^n + \mathbf{S}_{j-1/2}^n}{2} \right), \quad (11)$$

166 for $j = m \pm 1/2$. The full step solution is then defined from the intermediate

167 step values as

$$\mathbf{U}_m^{n+1} = \mathbf{U}_m^n - \frac{\Delta t}{\Delta x} \left(\mathbf{T}_{m+1/2}^{n+1/2} - \mathbf{T}_{m-1/2}^{n+1/2} \right) + \frac{\Delta t}{2} \left(\mathbf{S}_{m+1/2}^{n+1/2} + \mathbf{S}_{m-1/2}^{n+1/2} \right). \quad (12)$$

168 3.3.1. Bifurcation conditions

To ensure conservation each bifurcation is decomposed into a parent node and daughter nodes, as illustrated in Figure 4. At each branch bifurcation, continuity of pressure, and conservation of flow gives

$$Q_{b,j}^{p,M} = Q_{b,0}^{d_1,j} + Q_{b,0}^{d_2,j}, \quad (13)$$

$$P_{b,M}^{p,j} = P_{b,0}^{d_1,j} = P_{b,0}^{d_2,j}, \quad (14)$$

169 where p , d_1 and d_2 denote the parent and daughter nodes of the bifurcation,
170 and $j = n + 1/2, n + 1$.

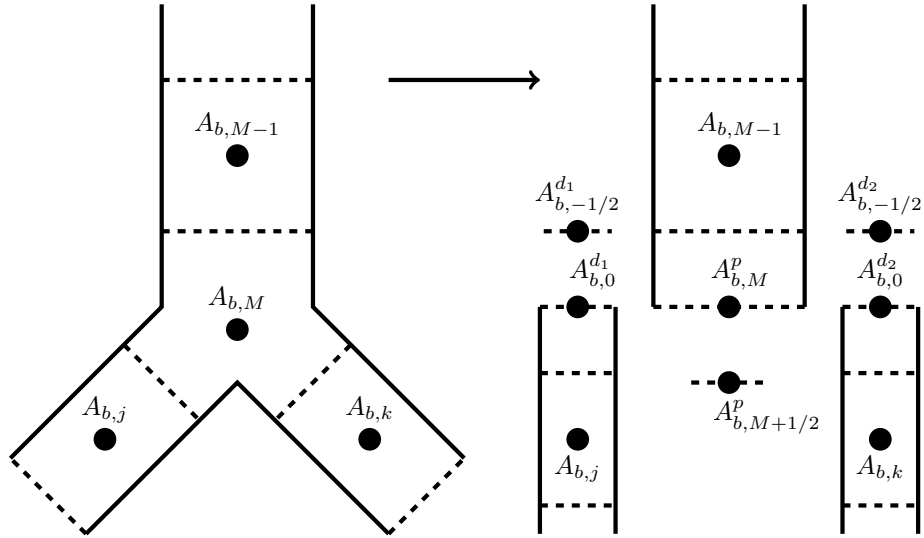


Figure 4: **Diagram of a 3-branch bifurcation decomposition.** The diagram shows a bifurcation before (left) and after (right) decomposition. New nodes d_1 and d_2 are created, alongside ghost node values $A_{b,-1/2}^{d_1}$, $A_{b,-1/2}^{d_2}$, and $A_{b,M+1/2}^p$. Similar nodes are also created for all corresponding Q_b values.

171 Given P_b is a function of A_b , the pressure continuity equation can be

172 re-written as

$$f_M^p \left(1 - \sqrt{\frac{A_{b,M}^{p,0}}{A_{b,M}^{p,n+1}}} \right) = f_0^{d_1} \left(1 - \sqrt{\frac{A_{b,0}^{d_1,0}}{A_{b,0}^{d_1,n+1}}} \right),$$

and similar for d_2 . These six continuity equations can be taken alongside the Lax-Wendroff scheme equations

$$A_{b,m}^{i,n+1} = A_{b,m}^{i,n} + \frac{\Delta t}{\Delta x} \left(\mathcal{T}_{1,m+1/2}^{i,n+1/2} + \mathcal{T}_{1,m-1/2}^{i,n+1/2} \right), \quad (15)$$

$$Q_{b,m}^{i,n+1} = Q_{b,m}^{i,n} + \frac{\Delta t}{\Delta x} \left(\mathcal{T}_{2,m+1/2}^{i,n+1/2} - \mathcal{T}_{2,m-1/2}^{i,n+1/2} \right) + \frac{\Delta t}{2} \left(\mathcal{S}_{2,m+1/2}^{i,n+1/2} + \mathcal{S}_{2,m-1/2}^{i,n+1/2} \right), \quad (16)$$

173 where $i = p, d_1, d_2$, and $m = M$ for p , and $m = 0$ for d_1 and d_2 .

This gives 12 equations, which govern the 12 state variables $Q_{b,m}^{i,j}, A_{b,m}^{i,j}$ for $i = p, d_1, d_2$, and $j = n, n+1$. However, these equations also require 6 variables which exist only as ghost nodes: $A_{b,M+1/2}^{p,n+1/2}, A_{b,-1/2}^{d_1,n+1/2}, A_{b,-1/2}^{d_2,n+1/2}$, and similar for Q_b . This requires 6 more equations to close the system, which are created by defining the ghost points through averaging, such that

$$Q_{b,m}^{i,n+1/2} = \frac{Q_{b,m-1/2}^{i,n+1/2} + Q_{b,m+1/2}^{i,n+1/2}}{2}, \quad (17)$$

$$A_{b,m}^{i,n+1/2} = \frac{A_{b,m-1/2}^{i,n+1/2} + A_{b,m+1/2}^{i,n+1/2}}{2}, \quad (18)$$

174 where $i = p, d_1, d_2$, and $m = M$ for p and $m = 0$ for d_1 and d_2 .

175 This gives rise to a closed non-linear system of 18 equations. However,
176 many of the equations are linear, meaning the system can actually be decom-
177 posed into two sets of smaller equation systems (more detail of this is given
178 in Appendix C).

179 The system outlined above is for a bifurcation with one parent and two
180 daughters. However, similar equation systems follow for other bifurcation
181 types (e.g. two parents one daughter, in the venous network, or one parent
182 and one daughter at the artery-capillary join).

183 *3.3.2. Inlet boundary condition*

At the two inlet boundaries (the left and right pulmonary arteries), a flow rate boundary condition is prescribed such that

$$\begin{aligned} Q_b(0, t) &= \frac{\bar{Q}_b t}{\tau} \exp\left(\frac{1}{2}(1 - t^2/\tau^2)\right), & 0 \leq t < H_T, \\ Q_b(0, t + jH_T) &= Q_b(0, t), & j = 1, 2, 3, \dots \end{aligned} \quad (19)$$

184 where \bar{Q}_b is the maximum flow, τ is the time of maximum flow, and H_T is
185 the heartbeat period.

186 We calculate the inflow boundary cross-sectional area, by first introducing
187 a ghost point $Q_{b,-1/2}^{n+1}$ which satisfies

$$Q_{b,0}^{n+1/2} = \frac{Q_{b,-1/2}^{n+1/2} + Q_{b,1/2}^{n+1/2}}{2},$$

188 where $Q_{b,0}^{n+1/2}$ is the inflow rate, evaluated at time step $n + 1/2$. Using this
189 ghost point, the inflow area A_b^0 can be calculated as

$$A_{b,0}^{n+1} = A_{b,0}^n - \frac{\Delta t}{\Delta x} \left(\mathcal{T}_{1,1/2}^{n+1/2} - \mathcal{T}_{1,-1/2}^{n+1/2} \right) + \frac{\Delta t}{2} \left(\mathcal{S}_{1,1/2}^{n+1/2} + \mathcal{S}_{1,-1/2}^{n+1/2} \right),$$

190 where $\mathcal{T}_{1,-1/2}^{n+1/2} = Q_{b,-1/2}^{n+1/2}$ and $\mathcal{S}_{1,-1/2}^{n+1/2} = 0$.

191 *3.3.3. Outlet boundary condition*

192 At each outlet boundary, we model the out of domain resistance and
193 compliance using a 3-element Windkessel model [26] with parameters \mathcal{R}_1 , \mathcal{R}_2 ,
194 and \mathcal{C}_t . This leads to the boundary model

$$\frac{\partial P_b}{\partial t} = \mathcal{R}_1 \frac{\partial Q_b}{\partial t} - \frac{P_b}{\mathcal{R}_2 \mathcal{C}_T} + \frac{Q_b(\mathcal{R}_1 + \mathcal{R}_2)}{\mathcal{R}_2 \mathcal{C}_T},$$

195 which is discretised using a Forward Euler method, as

$$P_{b,M}^{n+1} = P_{b,M}^n + \mathcal{R}_1(Q_{b,M}^{n+1} - Q_{b,M}^n) + \Delta t \left(-\frac{P_{b,M}^n}{\mathcal{R}_2 \mathcal{C}_T} + \frac{Q_{b,M}^n(\mathcal{R}_1 + \mathcal{R}_2)}{\mathcal{R}_2 \mathcal{C}_T} \right),$$

196 where

$$P_{b,M}^{n+1} = \frac{f_M}{\rho_b} \left(1 - \sqrt{\frac{A_{b,M}^0}{A_{b,M}^{n+1}}} \right).$$

197 A second equation is constructed through an upwind discretisation of Equa-
198 tion (9):

$$A_{b,M}^{n+1} = A_{b,M}^n - \frac{\Delta t}{\Delta x} (Q_{b,M}^{n+1} - Q_{b,M-1}^{n+1}).$$

199 These two equations are solved iteratively using Jacobi's method until a
200 convergent solution is reached (to a desired tolerance).

201 3.3.4. Computational implementation

202 The model outlined in the previous section is both highly non-linear and
203 extremely large. At a minimum, each branch in the system requires three
204 nodes (one at each end, and a central node), both with two unknown variables
205 (A_b, Q_b). This means at the lowest resolution for a full conducting airway
206 zone structure (approximately 100,000 branches, 50,000 of which are termi-
207 nal), the corresponding vasculature system has 250,000 arterial branches, and
208 thus 1,500,000 variables. While the Lax-Wendroff scheme is explicit, due to
209 conservation constraints each bifurcation (of which there are approximately
210 200,000) is constrained by 18 non-linear equations. In Appendix C we il-
211 lustrate how the computational challenges of the bifurcation conditions can
212 be reduced through careful algebraic manipulation; however, even with these
213 simplifications, the resulting system is incredibly large and computationally
214 intensive.

215 This is further exacerbated by the time step constraints imposed by the
216 explicit solution scheme. Assuming a uniform spatial discretisation over each
217 branch, it can be shown that the Lax-Wendroff method is stable [11] if the
218 associated Courant Friedrichs Lewy (CFL) condition is fulfilled:

$$\frac{\Delta t}{\Delta x} \leq \left| \frac{Q_b}{A_b} \pm c \right|^{-1},$$

219 for both choices of sign, where

$$c = \sqrt{\frac{A_b}{\rho_b} \frac{\partial P_b}{\partial A}},$$

Parameter	Value	Interpretation	Value taken from:
\mathcal{C}_T	$1.3 \times 10^{-6} \text{ cm}^4\text{s}^2/\text{g}$	Windkessel parameter	Olufsen [24]
D_{He}	$0.803 \text{ atm.cm}^2.\text{s}-1$	Diffusion rate for He in air	Marrero et al. [27]
D_{SF_6}	$0.102 \text{ atm.cm}^2.\text{s}^{-1}$	Diffusion rate for SF_6 in air	Marrero et al. [27]
D_{N_2}	$0.2 \text{ atm.cm}^2.\text{s}-1$	Diffusion rate for N_2 in air	Marrero et al. [27]
\mathcal{D}_{cap}	$5 \times 10^{-4} \text{ L/s/mmHg}$	Diffusing capacity of N_2	Average for O_2 and CO_2 Ben-Tal [4]
δ	0.1cm	Artery boundary layer size	Olufsen et al. [11]
H_T	1s	Heartbeat period	Standard value
k_1	$2 \times 10^7 \text{ g/s}^2\text{cm}$	Fit parameter for $f(R_b^0)$	Olufsen [24]
k_2	$-22.53 / \text{cm}$	Fit parameter for $f(R_b^0)$	Olufsen [24]
k_3	$8.65 \times 10^5 \text{ g/s}^2 \text{ cm}$	Fit parameter for $f(R_b^0)$	Olufsen [24]
ρ_b	1060 kg/m^3	Density of blood	Saladin and Porth [28]
\bar{Q}_b	$20\text{cm}^3/\text{s}$	Maximum inlet flow rate	Olufsen [24]
\mathcal{R}_1	$25300 \text{ g}/(\text{s cm}^4)$	Windkessel parameter	Olufsen [24]
\mathcal{R}_2	$13900 \text{ g}/(\text{s cm}^4)$	Windkessel parameter	Olufsen [24]
σ_b	$1.7 \times 10^{-5}/\text{mmHg}$	Solubility of N_2 in blood	Sander [29]
τ	0.1s	Time of peak inlet flow (during each heartbeat)	Olufsen [24]
$t_{\text{circulation}}$	60s	Average time taken for blood to circulate the body	Katz [30]
ν_b	$0.046 \text{ cm}^2/\text{s}$	Dynamic viscosity of blood	Olufsen et al. [11]

Table 1: **Pulmonary model parameters**

220 is the pulse wave speed.

221 In standard implementation on a full conducting zone structure, we have
222 found this leads to an average constraint condition of

$$\Delta t \leq 10^{-6}.$$

223 For non-trivial simulations of ventilation and gas transfer, a stable blood
 224 profile is needed for at least the duration of a breathing cycle. In practice, this
 225 means blood flow needs to be simulated for a duration of 3 breathing cycles
 226 (to allow for solution stabilisation), equating to 12 seconds at a standard
 227 breathing rate. Thus, total solution of the system requires explicit iteration
 228 of a system of approximately 1,500,000 variables more than 10^7 times with
 229 the Lax-Wendroff scheme.

230 In a standard CPU architecture this would be computationally intractable,
 231 with estimated runtime being greater than 1 year per profile. However, given
 232 that the solution scheme is explicit, the calculations (within each time step)
 233 are highly parallelisable. To exploit this structure, we solve the blood flow
 234 model in a GPU environment. A standard GPU (as of 2018) has between
 235 1000-4000 cores. This means that the incorporation of GPU computing could
 236 be expected to increase runtime by an order of $10^3 - 10^4$ (for a sufficiently
 237 large system). This was one of the primary motivations for the use of an ex-
 238 plicit solution scheme. The explicit scheme introduces a harsh time constraint
 239 penalty, but the use of high-performance computing greatly offsets this ef-
 240 fect. Equally, given the highly non-linear nature of the system (particularly
 241 the continuity constraints across each bifurcation), for accurate solution an
 242 implicit scheme would also be expected to require quite a small time step.
 243 However, an implicit scheme would not be able to be implemented in a GPU
 244 environment with the same degree of ease or effectiveness as the explicit
 245 scheme.

246 GPU implementation of the blood flow model was performed using *gpuAr-*
 247 *ray* structures within MATLAB's *Parallel Computing Toolbox*. All simu-
 248 lations of blood flow were computed using an Alienware 17 R2 laptop (i7
 249 processor, NVIDIA GTX970 GPU).

250 3.4. Blood gas transport model

251 Following calculation of bloodflow nad arterial cross-sectional area, these
 252 profiles are used to drive the convective transport equation

$$\frac{\partial A_b C_b}{\partial t} = \frac{Q_b}{A_b} \frac{\partial A_b C_b}{\partial x}, \quad (20)$$

253 where C_b is the gas concentration.

254 It should be noted that while A_b and Q_b appear in Equation (20), they
 255 can be solved independently of C_b . Given this, the model can be implemented

256 numerically using a similar approach to that given in Equation (7), setting
 257 $D = 0$.

258 At each outflow branch, during outward flow, concentration is removed
 259 from the branch, proportional to the flow rate, meaning

$$\frac{\partial C_b}{\partial \mathbf{n}} = \frac{Q_b}{A_b} C_b,$$

260 where \mathbf{n} is the outward normal vector to the boundary. During inward flow,
 261 it is assumed that no concentration of gas re-enters the system, such that

$$\frac{\partial C_b}{\partial \mathbf{n}} = 0.$$

262 At each inflow boundary, flow is only positive (due to the prescribed inflow,
 263 given in Equation (19)). Thus, there is one inflow condition of the form

$$\frac{\partial C_b}{\partial \mathbf{n}} = \frac{Q_b}{A_b} C_{\text{in}},$$

264 where C_{in} is the upstream gas concentration.

265 To create a closed system, gas which exits the pulmonary veins is brought
 266 back into the pulmonary arteries, via the equation

$$C_{\text{in}}(t) = \bar{C}_{\text{out}}(t - t_{\text{circulation}}), \quad (21)$$

267 where \bar{C}_{out} is the averaging outflow gas concentration, and $t_{\text{circulation}}$ is the
 268 average time it takes the gas to circulate the body (to get from the outflow
 269 point back to the inlet). Clearly this is a simplified model that could be
 270 updated to incorporate other factors such as tissue absorption, or chemical
 271 reactions within the body.

272 3.5. Alveolar-capillary transport model

To close the system, we link the two gas transport models, with a model
 for transfer across the alveolar-capillary membrane. Transport rates are as-

sumed proportional to the partial pressure gradient, such that [4]:

$$\frac{\partial V_{\text{acin}} C_{\text{acin}}}{\partial t} = \mathcal{D}_{\text{cap}}(P_{p,b} - P_{p,\text{acin}}), \quad (22)$$

$$\frac{\partial V_b C_b}{\partial t} = -\mathcal{D}_{\text{cap}}(P_{p,b} - P_{p,\text{acin}}), \quad (23)$$

where C_b is the concentration in the centre of the capillary, C_{acin} is the concentration in the associated acinar region, and \mathcal{D}_{cap} is the diffusing capacity (not to be confused with diffusion rate) of the gas across the alveolar-capillary membrane. $P_{p,b}$ and $P_{p,\text{acin}}$ are the partial pressures of the gas in blood and the acinus respectively, calculated as

$$P_{p,b} = \frac{1}{\sigma_b} C_b,$$

$$P_{p,\text{acin}} = P_{\text{acin}} C_{\text{acin}},$$

where σ_b is the solubility of the gas in blood, and P_{acin} is the gas pressure inside the acinus, which is the total pressure, minus the water vapour pressure (typically 47mmHg).

3.6. Total model

Combining the models outlined in the previous sections we can achieve simulation of gas transport throughout the entire pulmonary system. The process for this is described in Figure 5. Firstly, the ventilation profile and associated acinar volumes are calculated using System (2)-(5). The acinar volumes are then used to calculate capillary lengths with Equation (1), meaning the blood flow profile and arterial areas can be simulated through System (9)-(10). Once the ventilation and blood flow distributions are calculated, gas transfer is simulated using Equation (6) for the airways and Equation (20) for the bloodstream. Both of these equations are discretised using the same time step size, and at each time step are solved independently of each other. Between time steps, System (22)-(23) is used to account for gas transfer across the alveolar-capillary membrane.

Under an assumption of steady breathing and heart rate, ventilation and blood flow profiles are simulated over consecutive breathing cycles until stability (within 1%) is reached (typically taking 3 periods). These profiles are then repeatedly used to simulate gas transfer for as long as necessary. While

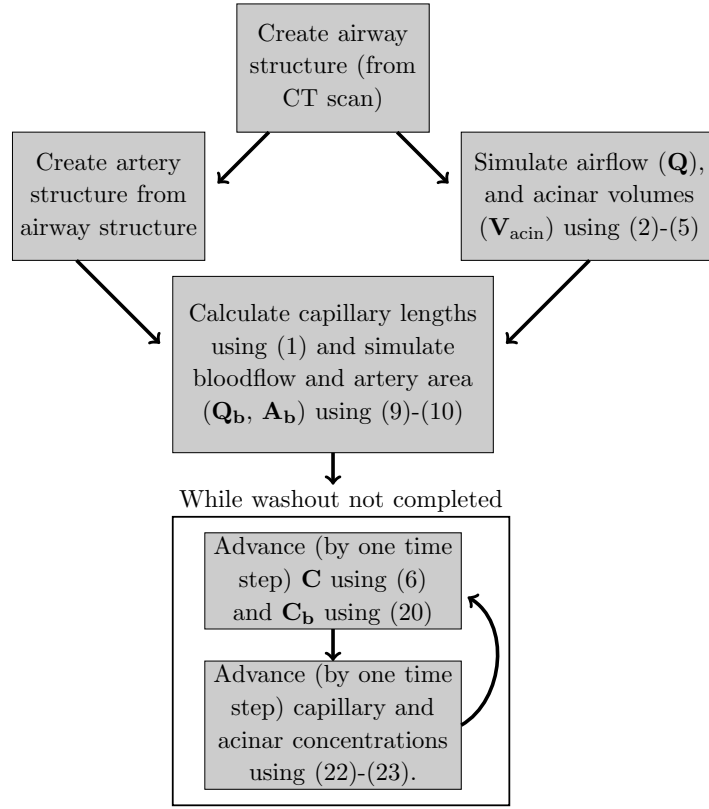


Figure 5: **Flow diagram for the pulmonary model solution procedure.**

in many applications gas transfer is simulated for a substantially longer period than blood flow, the solution speed is still dominated by the time taken to calculate the blood flow profile. This is because all other components of the model are solved implicitly, meaning time step sizes can be much larger ($\approx 10^{-2}$) than that of the explicit blood flow scheme ($\approx 10^{-6}$).

4. Results

4.1. Clinical validation

Given the complexity of the pulmonary model, a clear question to address is whether the model produces physically realistic, and clinically relevant results. Extremely detailed validation of the model throughout the entire pulmonary system is beyond the scope of a single study. Instead, we consider an array of experimental results within the literature.

311 A clear validation of the airways ventilation and transport components
 312 of the model was presented by Foy et al. [20]. Within this work, the airways
 313 model was shown to be able to sensitively capture inter-patient differences
 314 when simulating outputs from the multiple-breath washout (MBW). Pozin et
 315 al. [31] analysed a similar uni-directional, pressure-driven flow model (though
 316 coupled with a lung parenchyma model), showing accurate alignment with
 317 physical ventilation measurements.

318 Alongside this, the use of Navier-Stokes to simulate blood flow has un-
 319 dergone a variety of different experimental validations within the literature.
 320 In their initial presentation, Olufsen et al. [11] showed clear concordance
 321 between simulations of arterial blood flow, and experimental measurements.
 322 Other validations have been performed using full 3D simulation [32], with
 323 strong concordance between the 3D and 1D models [33, 34]. Effective valida-
 324 tion has also been performed in capillary networks [35], though this compared
 325 steady-state distributions only.

326 Convection-based models of oxygen transport in blood, similar to equa-
 327 tion (20) (though also accounting for haemoglobin binding) have also been
 328 applied within the literature, showing strong concordance with experimental
 329 measurements [36].

330 The wealth of prior validation of the individual components of the pul-
 331 monary model gives us confidence in its ability to meaningfully capture the
 332 dominant mechanics of the pulmonary system. Clearly there would be value
 333 to validation of the model in a combined, holistic setting. We see this as a
 334 clear avenue for future research.

335 4.2. Comparing different washout gases

336 To illustrate the potential value of efficient pulmonary simulation, we
 337 apply the model to a clinically relevant question concerning the multiple-
 338 breath washout [37]. The MBW is a pulmonary function test that uses
 339 measurements of ventilation heterogeneity at the mouth, to make inferences
 340 about the presence of lung disease. Typically the test is performed in one of
 341 two ways; either air mixed with an inert-gas (such as SF₆ or ³He) is washed-
 342 in by the subject (breathed in until it is assumed to have equilibrated in
 343 the lungs), and then washout of the inert gas is performed by switching the
 344 subject back to an air mixture without the gas; or in the case of nitrogen
 345 washouts, since N₂ is already present in air, no wash-in is performed, and
 346 instead a washout is performed using pure oxygen.

347 Despite a wide variety of clinical [38, 39, 40] and computational [3, 20]
 348 studies of the inert-gas washout, there is a lack of clear understanding as to
 349 how the choice of tracer gas may affect outputs [37]. Some recent studies
 350 have investigated this phenomenon [39], showing a potential bias between
 351 different gases. However, this finding hasn't been illustrated broadly enough
 352 to allow for consensus.

353 To help address this gap, we apply the pulmonary model to simulate the
 354 effect of tracer gas choice on MBW outputs, using the three most common
 355 tracer gases (SF_6 , ^3He , and N_2). Simulations were performed using each
 356 of the 26 patient-based lung structures. Each simulation was performed
 357 in an orthostatic position, after artificially washing in the tracer gas, at a
 358 concentration of 4% for SF_6 and ^3He , and 78% for N_2 . Diffusion rates for
 359 each gas are given in Table 1, and for SF_6 and ^3He , \mathcal{D}_{cap} was set to 0. For each
 360 simulation we calculate the washout indices LCI (Lung Clearance Index) and
 361 s_{cond} , with precise definitions of each given in prior studies in the literature
 362 [2, 40].

363 As an initial step, in Figures 6 and 7 we present flow, cross-sectional area,
 364 and N_2 concentration profiles at various locations throughout the pulmonary
 365 system, in a healthy lung structure. Considering the blood flow profile, we
 366 see small alternations in peak flow values every four heartbeats, due to the
 367 expansion and contraction of the capillaries in response to the alveoli. We
 368 also note that the arterial area profile behaves similarly to the flow profile,
 369 but has a slight offset of a few fractions of a second.

370 Considering Figure 7 no immediately obvious effect of the bloodstream
 371 can be seen in the tracheal N_2 concentration profile. This is to be expected
 372 though, given that the individual contributions from the capillaries will be
 373 smoothed out by the time they reach the trachea. We see expected behaviour
 374 in the left pulmonary artery gas concentration profile, with an offset time of
 375 just over 60 seconds, corresponding to the imposed mean circulation time.
 376 Interestingly, the pulmonary artery empties at a much slower rate than the
 377 shown capillary. This is due to accumulation effects, and that flow in the cap-
 378 illaries is not perfectly synchronous (similar to the acinar regions). Finally,
 379 we note that before the washout begins, gas concentrations in the capillaries
 380 stabilise to just under 1%, while concentrations in the acinus stabilised at
 381 78%. This is in line with the normal physiological concentration of nitrogen
 382 in the bloodstream, when breathing standard air (78% nitrogen).

383 Within Figures 8 and 9, we compare simulated s_{cond} and LCI values,
 384 using the three different tracer gases. Firstly, comparing the non-pulmonary

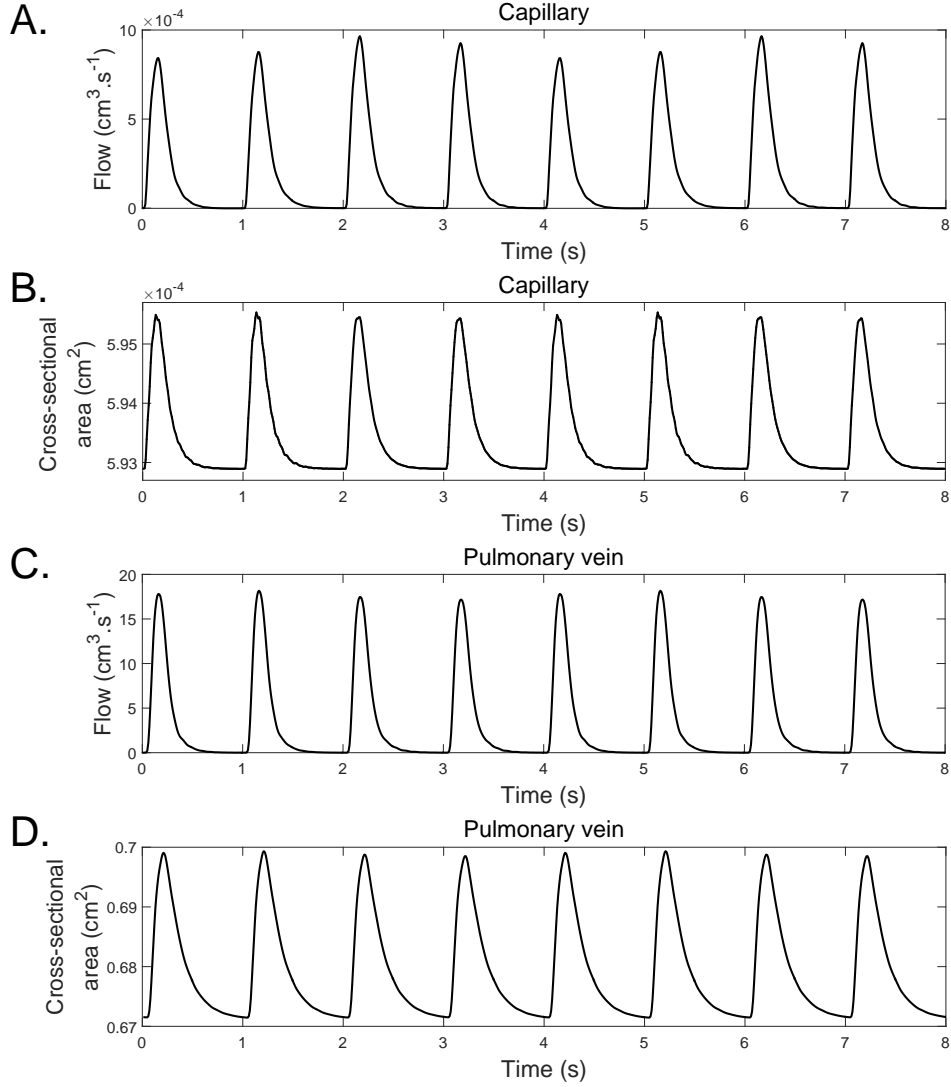


Figure 6: **Blood flow and cross-sectional area profiles in a capillary (A,B) and pulmonary vein (C,D).** The capillaries undergo a strong sinusoidal pattern in peak values, driven by the expansion and contraction of the acinus. Flow is significantly larger in the pulmonary arteries, which also undergo a more significant cross-sectional area deformation.

diffusive gases, we see that there is a very slight negative bias in both LCI
and s_{cond} when using ^3He . This is potentially due to the higher diffusivity of
helium, which would allow constricted areas of the lung to washout slightly

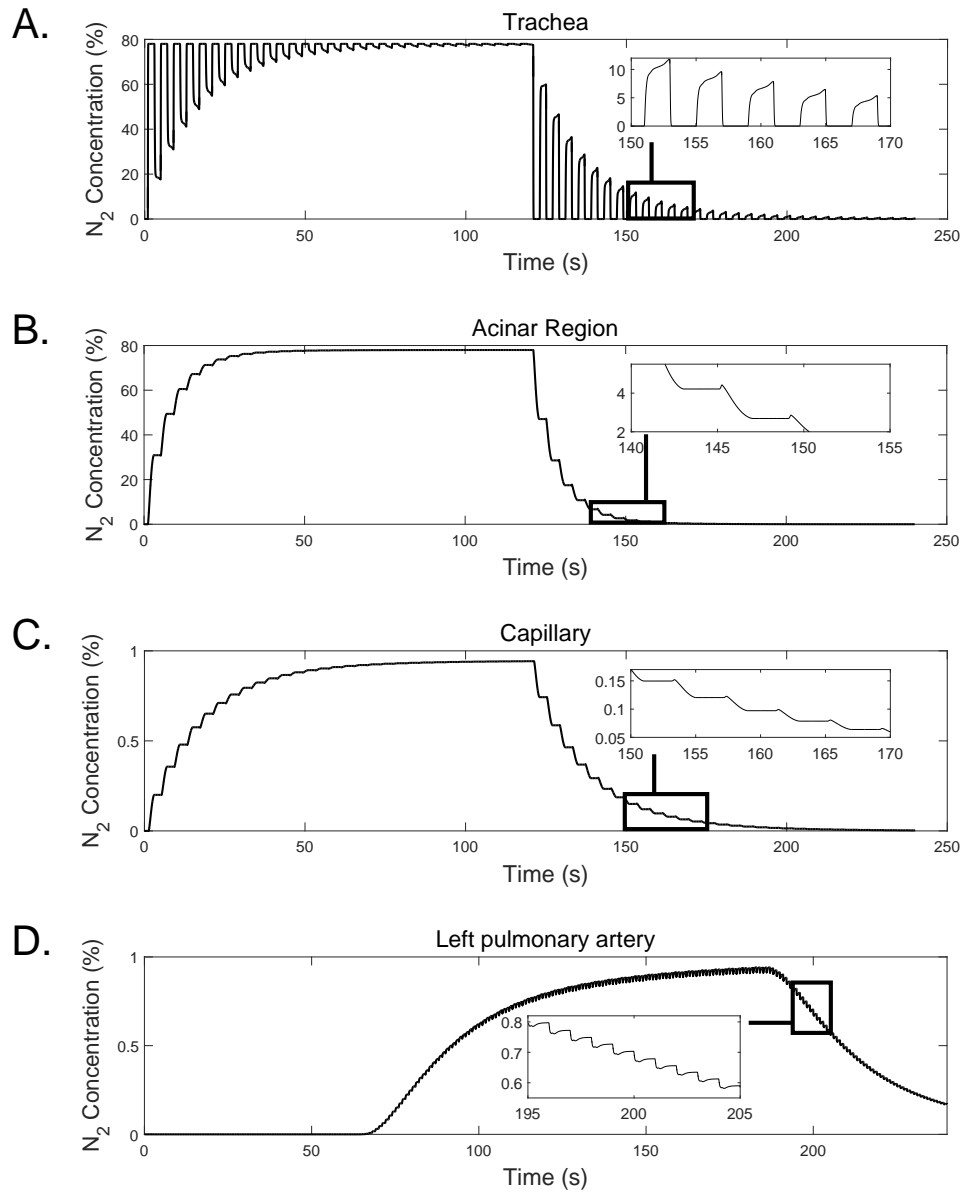


Figure 7: **Concentration profiles at various locations in the pulmonary network.** Nitrogen concentrations can be seen during wash-in and washout at the trachea (A), in an acinar region (B) and its associated capillary (C), and in the left pulmonary artery (D). For each washout profile, a zoom in is given to show behaviour over a few breaths.

388 faster. However, the confidence intervals for these differences greatly overlap

389 zero, meaning the inference is quite weak.

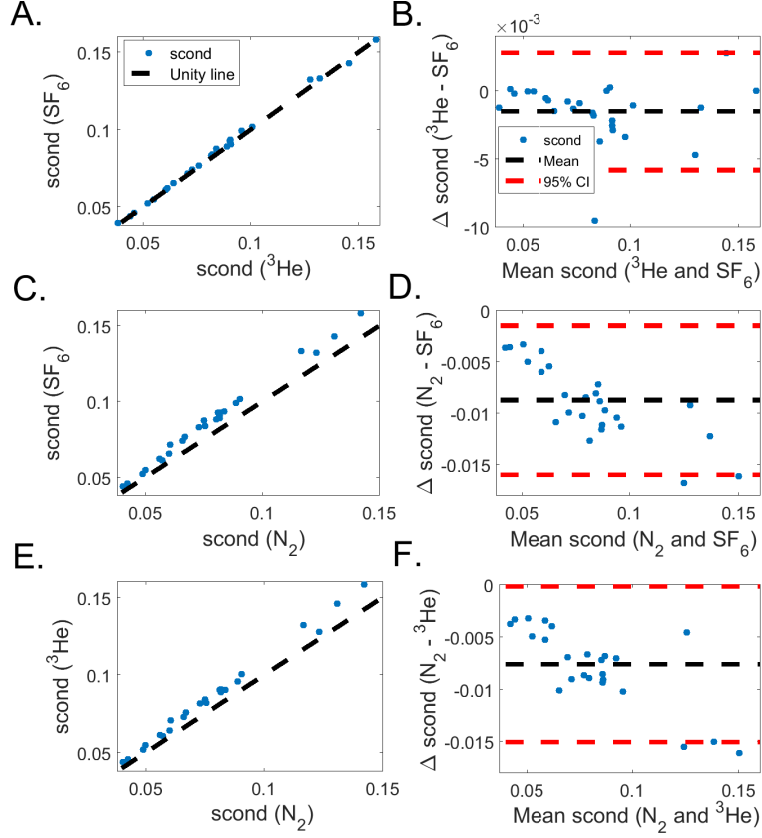


Figure 8: **Comparison of simulated s_{cond} with different tracer gases.** Results comparing ^3He , SF_6 and N_2 are shown, with a line of best fit (A,C,E) and Bland-Altman plots (B,D,F) given.

390 Comparing N_2 washouts to ^3He and SF_6 washouts, the differences appear
 391 much more consistent. In both cases s_{cond} has a noticeable negative bias,
 392 and LCI a positive bias, with magnitude of difference increasing with the
 393 index value. While small, this bias appears consistent, with 95% confidence
 394 intervals excluding zero.

395 4.3. Error convergence

396 To close the results section, we briefly illustrate error convergence of the
 397 model. Due to the model complexity, deriving analytical solution profiles is

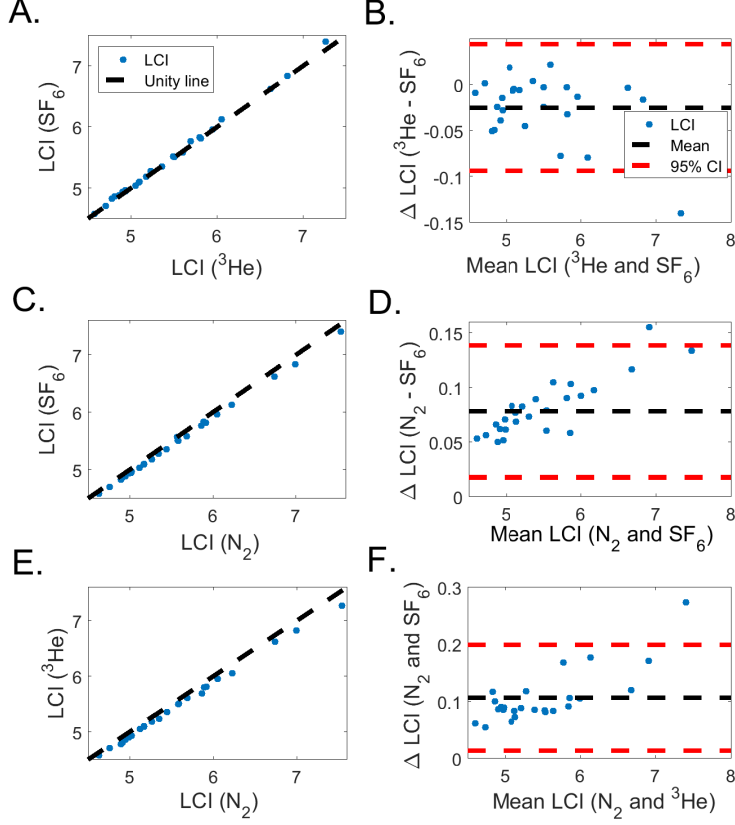


Figure 9: **Comparison of simulated LCI with different tracer gases.** Results comparing ^3He , SF_6 and N_2 are shown, with a line of best fit (A,C,E) and Bland-Altman plots (B,D,F) given.

398 infeasible. Instead, we analyse error convergence of the model under simul-
 399 taneous temporal and spatial refinement of the domains. We first define the
 400 error of a solution \mathbf{x} , relative to a fine mesh solution, \mathbf{x}_{fine} , such that

$$\text{err} = \max \left| \frac{\mathbf{x} - \mathbf{x}_{\text{fine}}}{\mathbf{x}_{\text{fine}}} \right|.$$

401 Note that to avoid catastrophic cancellation, solution error is only calculated
 402 at points where the elements of \mathbf{x}_{fine} are sufficiently different from 0.

403 Due to computational constraints, error was analysed in an artificially
 404 created 3 generation, and 5 generation pulmonary network, corresponding to
 405 a pulmonary structure with 28 and 78 branches respectively. Each generation

406 started with a trachea of radius 1cm and length 10cm. To grow the tree, at
 407 each bifurcation point, two new branches were created, at branch angles of
 408 $\pm 30^\circ$, with radius and branch length reduction factors of 0.8 and 0.6. As
 409 an example, this leads to a branch length and radius of 6cm and 0.6cm
 410 at generation 2, 4.8cm and 0.36cm at generation 3, and so on. To add
 411 assymetry to the tree, each branch length and radius was multiplied by a
 412 normal-random number, drawn from the distribution $\mathcal{N}(1, 0.05)$. The 3-
 413 generation and 5-generation airway tree structures are illustrated in Figure
 414 10.

415 Blood flow and cross-sectional area profiles (over 12 seconds) for the 3
 416 generation network were calculated at the centre node of each branch (in
 417 arteries, capillaries and veins) with 1, 3, 7, 15, and 31 nodes per branch,
 418 and corresponding dt values of 0.002, 0.001, 0.0005, 0.00025, 0.000125. Error
 419 was calculated as the maximum relative difference between the solution and
 420 the corresponding fine mesh solution at all branch bifurcations, and centre
 421 nodes. The fine mesh solution was created using 63 nodes per branch, and
 422 $dt = 0.0000625$. A similar process was applied to analyse error in the 5
 423 generation network, using $dt = 0.0002, 0.0001, 0.00005, 0.000025$ and 1, 3, 7
 424 and 15 nodes per branch, and a fine mesh solution created with 31 nodes per
 425 branch, and $dt = 0.0000125$. The convergence of error in the structures can
 426 be seen in Figure 10. The convergence appears linear, as is expected from
 427 the Lax-Wendroff scheme.

428 A similar approach was applied to analyse convergence of the gas trans-
 429 port model. Simulations of a 30s N_2 washout (preceded by a 30s N_2 wash-in)
 430 were performed in a 3 and 5 generation network, with the same pairs of dt
 431 and number of nodes as above. The discretisation was applied to both the
 432 blood flow and concentration model, across the airways and arterial network.
 433 The error convergence is shown in Figure 11, appearing linear as expected.

434 5. Discussion

435 We have presented the design and implementation of a gas transport
 436 model for the entire pulmonary system, alongside preliminary results from
 437 simulation of the multiple-breath nitrogen washout. Here we provide a brief
 438 discussion of clinical relevance, computational considerations, limitations,
 439 and potential future work.

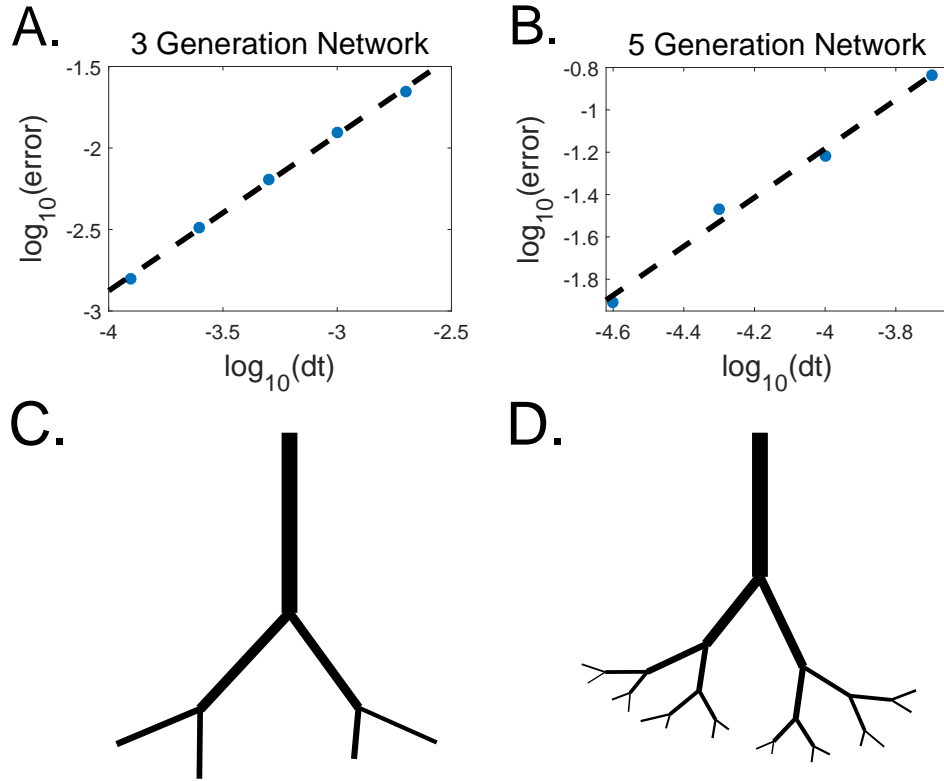


Figure 10: **Error convergence of the blood flow model in a 3 generation network (A, C), and a 5 generation network (B, D).** Both error plots have slopes of approximately 1, indicating linear convergence. Visualisation of the airway tree is also given, with line thickness corresponding to radius (C, D).

440 5.1. Clinical relevance

441 The results in Figures 8 and 9 suggest that the bloodstream interactions
 442 of nitrogen lead to a clear and consistent bias in washout indices; causing an
 443 elevation in LCI and reduction in s_{cond} . The positive bias of LCI using N_2
 444 confirms nicely with the clinical results of Jensen et al. [39] who showed that
 445 LCI was elevated when using N_2 , comparative to SF_6 , with the magnitude
 446 of difference increasing in the presence of cystic fibrosis. This result is fur-
 447 ther confirmed when comparing reference values for healthy controls, across
 448 various studies using different tracer gases [38]. However it should be noted
 449 that, to the best of our knowledge, no single prior study has illustrated this

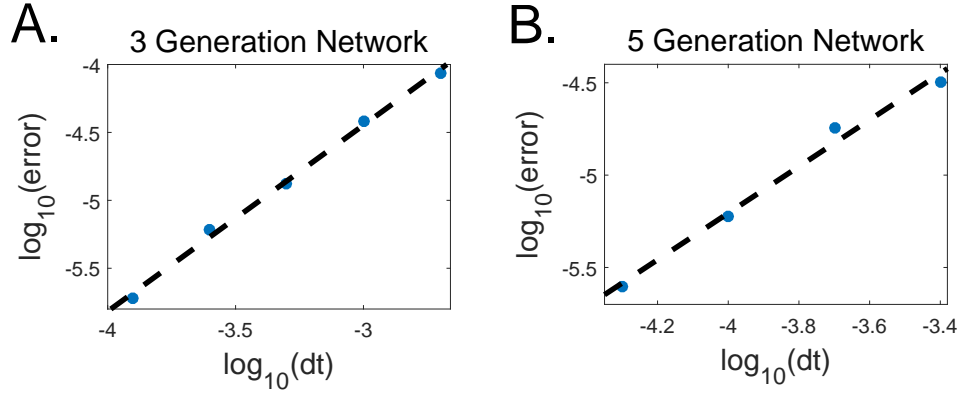


Figure 11: **Error convergence of the pulmonary model in a 3 generation network (A), and a 5 generation network (B), over the arteries, acinar regions and airways.** The two error plots have slopes of approximately 1.2-1.4, indicating linear convergence (as expected).

phenomenon within an asthmatic patient group. Thus, the results in this study help to provide evidence for the general nature of this phenomenon, beyond being specific to cystic fibrosis.

While there are some results in the literature comparing LCI, to the best of our knowledge, there are no large clinical studies which compare s_{cond} under different gas choices. The results here suggest that the bias of s_{cond} is opposite to that of LCI, with N_2 leading to a reduction in the index, comparative to SF_6 , and ^3He . Similar to LCI, this bias is quite small, however, it appears consistent, potentially allowing for correction when comparing clinical results obtained using different gases.

5.2. Computational constraints

As outlined previously, the computational scale of the model is quite large. To calculate the blood flow and arterial cross-sectional area profiles over 12 seconds, a system of approximately 1,500,000 variables was iteratively solved 10^7 times. More generally, if we have an N generation network, the number of branches can be approximated by 2^N , leading to 2^{N+1} branches in the associated arterial network (excluding the capillaries). Assuming that only bifurcations occur (no trifurcations), and using the most coarse discretisation possible, each arterial branch contains 14 variables (two at the branch centre, 4 at each branch end, and 2 ghost nodes at each branch end). If each terminal bronchiole is subtended by a single acinus with a single capillary, there are

471 2^{N-1} total capillaries, each also having 14 variables. This leads to a total
 472 system complexity of

$$\mathcal{O}(14(2^{N+1} + 2^{N-1})).$$

473 Further to this, the time step constraint on the Lax-Wendroff scheme scales
 474 linearly with the branch length (which directly relates to Δx). Assuming a
 475 branch length scaling factor of 0.6 (approximated from histological data [18]),
 476 as the tree grows, the total number of time steps scales according to 1.65^N .
 477 For a 2 generation system, with a physically realistic geometry, we estimated
 478 a necessary step size of $\Delta t = 10^{-3}$, leading to approximately 10^4 steps per
 479 solution (of a 12 second blood profile). Given this, the total complexity of
 480 the model (expressed as number of necessary variable-iterations) is

$$\mathcal{O}(14(2^{N+1} + 2^{N-1}) \times 10^4 1.65^N) \approx \mathcal{O}(10^5 \times 2^{1.72N+1}).$$

481 For a full respiratory system ($N \approx 23$), this would lead to approximately
 482 10^{17} variable iterations. In practice this number is much greater, as beyond
 483 generation 16-17 the assumption of each branch being subtended by a sin-
 484 gle acinus fails to hold. Regardless, this presents significant computational
 485 strain, which we illustrate by comparing run times with and without GPU
 486 implementation, for various tree sizes (Figure 12).

487 5.3. Limitations

488 Models for pulmonary blood flow are not a completely recent development
 489 within the literature. However, most applications have been strongly limited
 490 by available computing power, and as such use simple approximations for
 491 flow in the capillaries and small arteries, and often exclude any venous com-
 492 ponent. As we have shown, through the embedding of the blood flow models
 493 in efficient parallel environments, many of these computational limitations
 494 may be overcome, allowing for effective simulation of the pulmonary system
 495 to much deeper levels.

496 Clearly though, this model still applies a variety of simplifying approxi-
 497 mations, to make simulation at this depth computationally tractable. One of
 498 the strongest limitations of the model is the simplicity of the respiratory zone
 499 approximation. Representation of all veins and arteries below the structural
 500 resolution by a single capillary is clearly not physically realistic. However,
 501 this is primarily driven by a lack of realistic structural information and com-
 502 putational constraints. With access to more powerful HPC environments,

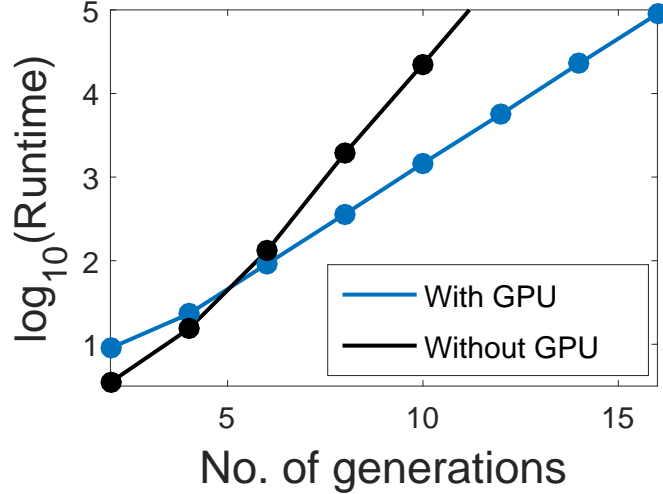


Figure 12: **Comparison of runtimes when simulating blood flow with and without a GPU architecture.** Run times are given for arterial trees with generation sizes 2-16

503 and improvements in imaging techniques (such as micro-CT [41]), these lim-
504 itations may be overcome.

505 Beyond this, the model is 1D in nature, meaning it cannot account for tur-
506 bulent effects in both air and blood flow. Again, this choice is primarily made
507 due to computational constraints. Given that both airflow and blood flow
508 drastically slow as airway and artery radii decrease, we do not believe that
509 the 1D approximation significantly affects accuracy. However, in the airflow
510 and blood flow literature some groups have taken a multi-scale approach,
511 whereby the largest branches are modelled using a full 3D Navier-Stokes,
512 before transitioning to 1D, past a certain point [42, 5].

513 Another limitation is the assumption of a linear stress-strain relationship
514 between pressure and arterial cross-sectional area. Given the reduction in
515 size and flow rates in the capillaries, the assumption of Newtonian flow may
516 not be perfectly valid. This assumption was made to allow for tractability
517 of the system. The investigation of tractable approaches to accounting for
518 non-Newtonian flow behaviour in the capillaries is a clear avenue for future
519 research.

520 Further to this, the model uses parameterised inflow and outflow bound-
521 ary conditions for blood flow. While we have applied a simplistic model for

inflow (Equation (19)), this could clearly be replaced with patient-specific data, or used to represent more complex scenarios (as would be caused by various heart conditions). Equally, the outlet boundary is parameterised by a Windkessel model, with 3 degrees of freedom ($\mathcal{R}_1, \mathcal{R}_2, \mathcal{C}_T$), using values from a prior study in the literature [24]. However, in future work, investigations could be undertaken to improve the outlet boundary condition, and create more accurate estimations of downstream resistance and compliance.

Considering the arterial boundaries, the model for gas transfer also uses a simplistic approximation of gas circulation throughout the entire body, parameterised by a mean circulation time $t_{\text{circulation}}$. This is a simple approximation made to allow for closure of the model. More complex models that account for tissue absorption, and chemical reactions could be implemented if relevant experimental information was available.

Finally, the models were applied using pulmonary networks which were directly modelled based off of the CT-generated airway structures, as opposed to an independent CT-generated artery/vein network. While the pulmonary arteries and veins closely follow the airway structure, this is not a perfect correspondence. We note though that this does not represent a limitation of the model itself, which in the presented form may be applied to any given 1D airway and pulmonary structure.

While the outlined limitations may seem significant, they should be interpreted in context of the computational considerations. The majority of these limitations are not inherent to the model, but simply chosen factors (termination depths, etc.) based on computational constraints. Given the parallelisable nature of the model, advancements in computing power may allow many of these limitations to be overcome. The investigation of more complex and physically realistic approximations is a clear avenue for future work.

5.4. Future work

Within this study we have only illustrated the application of the pulmonary model to simulation of N_2 gas transport. Adaptation of the model to a wider range of scenarios can be easily achieved though, with simple modifications.

The pulmonary model we have outlined is suitable for modelling transport of gases which cross the alveolar-capillary membrane, but which otherwise do not strongly interact with body tissues, or do so through a simple diffusive process. This means that the model in its current form cannot be

559 applied to model the two gases of highest interest in respiration; oxygen and
 560 carbon dioxide. However, adaptation of the model into this scenario is fairly
 561 straightforward, by building on prior work in the literature, such as that of
 562 Ben-Tal [4]. For the simulation of oxygen transport, the alveolar-capillary
 563 exchange model can be modified to account for haemoglobin binding and
 564 saturation such that

$$\frac{\partial V_b C_b}{\partial t} = \mathcal{D}_{\text{cap}} (P_{p,b} - P_{p,\text{acin}}) - N_0 T_h V_b \frac{dS}{dt},$$

565 where C_b is the oxygen concentration, N_0 is the maximum number of molecules
 566 of O_2 that can bind to haemoglobin, T_h is the haemoglobin concentration, and
 567 $S(T)$ is the saturation function of oxygen in haemoglobin. Various different
 568 forms for the saturation function exist within the literature [4].

569 Ben-Tal [4] also presented similar models for transport of CO_2 in the
 570 blood. However, to simulate both O_2 and CO_2 transfer across the pulmonary
 571 system, the model would need to be further expanded to incorporate a res-
 572 piration model, which decomposes O_2 into CO_2 . This could be incorporated
 573 by making the O_2 and CO_2 loss functions dependent on CO_2 and O_2 con-
 574 centration, with parameters inferred from the aerobic respiration chemical
 575 reaction.

576 If these adaptations were applied to the model, it would potentially be
 577 capable of realistically simulating a much larger variety of physical scenarios,
 578 and to more precisely probe disease processes, and pulmonary function tests.
 579 The potential uses for such a model are quite vast, as there is still a strongly
 580 limited understanding of how different morphological changes across both
 581 the airway and veins/arteries affect the overall function of the pulmonary
 582 system. The model could be applied to variety of questions such as investi-
 583 gating how pulmonary arterial wall thickness increases (as can be seen due
 584 to high cholesterol) affect the O_2 distribution across the lungs, or how an
 585 elevated heart rate may affect clinical respiratory measurements. This array
 586 of questions forms an exciting direction for future research within the field
 587 of computational modelling of the human body and the pulmonary system.

588 Acknowledgements

589 BF is funded by the Rhodes Trust.

590 This work was partially funded by an EU Framework 7 grant, through
 591 the AirPROM consortium.

592 Appendix A. Derivation of capillary length formula

593 Within the methods, we present a formula for capillary length, relative
 594 to volume of the acinus it surrounds (Equation (1)). Here we derive this
 595 formula.

596 For computational tractability, we aim to approximate the capillary bed
 597 surrounding each acinus by a single capillary. For this to be a reasonable
 598 approximation, we need the mass of blood in a single capillary to approximate
 599 the mass of blood in the corresponding capillary bed. To achieve this, we
 600 assume that the single capillary wraps around the surface area of the acinus,
 601 covering a fraction f . This means that the capillary length is proportional
 602 to surface area, but also limited by its own diameter (which determines how
 603 much of the surface any piece of the capillary covers). Combining these two
 604 dependencies gives

$$l_{\text{cap}} = f \frac{4\pi R_{\text{acin}}}{2R_{\text{cap}}^0} = f \frac{2\pi R_{\text{acin}}}{2R_{\text{cap}}^0}.$$

605 The fraction f of covered surface can be estimated by assuming a healthy
 606 adult lung (FRC= 2.5L) is surrounded by 60mL of capillary blood (a normal
 607 healthy adult value). Using a healthy lung from the Bordas set, this gives
 608 $f \approx 1/5$, meaning

$$l_{\text{cap}} = \frac{2\pi R_{\text{acin}}^2}{5R_{\text{cap}}^0}.$$

609 For this approximation to be appropriate, the ratio of lung volume to capil-
 610 lary blood should be independent of the number of generations in the airway
 611 tree. This is because this ratio significantly determines how strongly gas
 612 concentrations in the blood can affect concentrations in the airway (due to
 613 relative mass differences). To analyse whether this holds within our model,
 614 we first note that

$$V_{\text{cap}} = l_{\text{cap}} \times A_{\text{cap}} = \frac{2}{5}\pi^2 R_{\text{acin}}^2 R_{\text{cap}}^0,$$

615 where V_{cap} is the volume of the capillary, and A_{cap} is its cross-sectional area.

616 For a structure with a given FRC, approximated using an N -generation
 617 network, we assume there is an average ratio between capillary volume and
 618 acinus volume, such that

$$V_{\text{cap},N} \approx k V_{\text{acin},N},$$

619 where the subscript N denotes that the variable is from the N -generation
620 network. If we take this structure, and add another generation, but hold
621 FRC constant we have

$$V_{\text{acin},N+1} \approx \frac{1}{2} V_{\text{acin},N},$$

$$R_{\text{acin},N} \approx \left(\frac{1}{2}\right)^{1/3} R_{\text{acin},N},$$

623 as the number of acinar regions should approximately double in the new
624 network.

625 If we assume that at each generation, the capillary and airway radii de-
626 crease with a branching factor b_f , we also have

$$R_{\text{cap},N+1} \approx b_f R_{\text{cap},N},$$

627 which means that the new capillary volume can be approximated as

$$V_{\text{cap},N+1} \approx \frac{2}{5} \pi^2 b_f \left(\frac{1}{2}\right)^{2/3} R_{\text{acin},N}^2 R_{\text{cap},N}^0.$$

$$V_{\text{cap},N+1} \approx b_f \left(\frac{1}{2}\right)^{2/3} V_{\text{cap},N}.$$

629 If we assume the ratio between capillary volume and acinar volume is the
630 same for both sized networks, we have that

$$b_f \left(\frac{1}{2}\right)^{2/3} = \frac{1}{2},$$

631 which means that the branching factor must be

$$b_f = 2^{-1/3} \approx 0.79.$$

632 This number is the well-known optimal branching factor [43] for the human
633 lung, also known as the Hess-Murray law.

634 This illustrates that in an idealised branching network, this model holds,
635 and accurately maintains an appropriate ratio (which we have set from stan-
636 dard physiological values as 2500L: 60mL) between FRC and capillary blood
637 volume. In an actual lung, average branching factors are usually slightly
638 higher than the optimal factor, usually being around 0.81-0.86 [44]. Thus in

639 practice for airway networks significantly larger or smaller than 16 genera-
 640 tions, the surface area factor f should be modified to maintain this ratio.

641 Appendix B. Comparison of different alpha values

642 The bloodflow model (equations (9)-(10)) contains a parameter α , which
 643 accounts for the flow profile shape through the arterial cross-section. Results
 644 within this study have used the value $\alpha = 1$, corresponding to a flat profile.
 645 For completeness, within Figure B.13 we compare flow and arterial area
 646 profiles using $\alpha = 1.1$, a value commonly used within the literature [12]
 647 corresponding to a parabolic profile shape. As the figure shows, while α does
 648 influence overall behaviour, this change is fairly small, causing small shifts
 649 in peak values, and start times of the pulsatile behaviour. Given this, we do
 650 not believe that the choice of $\alpha = 1$ significantly biases the results in this
 651 study.

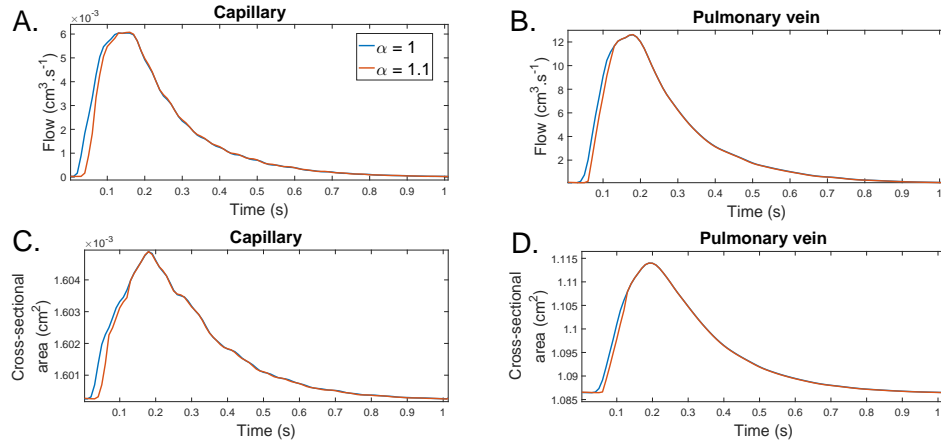


Figure B.13: **Comparison of flow and area profiles using $\alpha = 1$ and $\alpha = 1.2$.** As can be seen, the increase in α appears to only cause small shifts to overall profile behaviour in both peak flow and area values, and start time of the pulsatile behaviour.

652 Appendix C. Simplification of bifurcation equations

To simplify the bifurcation equations (in the blood flow model), we first introduce notation for the variables:

$$\begin{aligned}
x_1 &= Q_{b,M}^{p,n+1}, & x_2 &= Q_{b,M}^{p,n+1/2}, & x_3 &= Q_{b,M+1/2}^{p,n+1/2}, \\
x_4 &= Q_{b,0}^{d_1,n+1}, & x_5 &= Q_{b,0}^{d_1,n+1/2}, & x_6 &= Q_{b,-1/2}^{d_1,n+1/2}, \\
x_7 &= Q_{b,0}^{d_2,n+1}, & x_8 &= Q_{b,0}^{d_2,n+1/2}, & x_9 &= Q_{b,-1/2}^{d_2,n+1/2}, \\
x_{10} &= A_{b,M}^{p,n+1}, & x_{11} &= A_{b,M}^{p,n+1/2}, & x_{12} &= A_{b,M+1/2}^{p,n+1/2}, \\
x_{13} &= A_{b,0}^{d_1,n+1}, & x_{14} &= A_{b,0}^{d_1,n+1/2}, & x_{15} &= A_{b,-1/2}^{d_1,n+1/2}, \\
x_{16} &= A_{b,0}^{d_2,n+1}, & x_{17} &= A_{b,0}^{d_2,n+1/2}, & x_{18} &= A_{b,-1/2}^{d_2,n+1/2}.
\end{aligned}$$

We then define

$$\begin{aligned}
B_{M+1/2}(x) &= \frac{R_{b,M+1/2}^0 f}{\rho_b} \sqrt{A_{b,M+1/2}^0}, \\
F_{M+1/2}(x_1, x_2) &= -\frac{2\pi\nu_b R_{b,M+1/2}^0}{\delta} \frac{x_1}{x_2}, \\
\frac{dB_{M+1/2}}{dx}(x) &= \left(\frac{\partial B}{\partial R_b^0} \frac{dR_b^0}{dx} \right)_{M+1/2}^{n+1/2} \\
&= \left(2\sqrt{x} \left(\sqrt{\pi} f R_b^0 + \sqrt{A_b^0} \frac{df}{dR_b^0} \right) - A \frac{df}{dR_b^0} \right)_{M+1/2} \left(\frac{dR_{b,M+1/2}^0}{dx} \right), \\
\theta_i &= \frac{\Delta t}{\Delta x_i}, \\
\gamma &= \frac{\Delta t}{2}.
\end{aligned}$$

653 Using this notation, we can rewrite Equations (13)-(18) in the form

$$\mathbf{H}(\mathbf{X}) = \mathbf{0},$$

where $\mathbf{X} = (x_1, x_2, \dots, x_{18})^T$, and $\mathbf{H} = (h_1, h_2, \dots, h_{18})^T$. The vector \mathbf{H} comprises the 18 residual functions, with the equations for conservation of

flow (13):

$$h_1 = x_1 - x_4 - x_7, \quad (C.1)$$

$$h_2 = x_2 - x_5 - x_8, \quad (C.2)$$

the ghost node approximations (17)-(18):

$$h_{3,4,5} = x_{2,5,8} - \frac{x_{3,6,9}}{2} + k_{1a,1b,1c}, \quad (C.3)$$

$$h_{6,7,8} = x_{11,14,17} - \frac{x_{12,15,18}}{2} + k_{2a,2b,2c}, \quad (C.4)$$

$$\begin{aligned} k_{1a} &= -\frac{Q_{b,M-1/2}^{p,n+1/2}}{2}, \\ k_{1b} &= -\frac{Q_{b,1/2}^{d_1,n+1/2}}{2}, \quad k_{1c} = -\frac{Q_{b,1/2}^{d_2,n+1/2}}{2}, \\ k_{2a} &= -\frac{A_{b,M-1/2}^{p,n+1/2}}{2}, \\ k_{2b} &= -\frac{A_{b,1/2}^{d_1,n+1/2}}{2}, \quad k_{2c} = -\frac{A_{b,1/2}^{d_2,n+1/2}}{2} \end{aligned}$$

advancement of A_b in time (15):

$$h_9 = x_{10} + \theta_p x_3 - k_{3a}, \quad (C.5)$$

$$h_{10,11} = x_{13,16} - \theta_{d_1,d_2} x_{6,9} - k_{3b,3c}, \quad (C.6)$$

$$k_{3a} = A_{b,M}^{p,n} + \theta_p Q_{b,M-1/2}^{p,n+1/2},$$

$$k_{3b} = A_{b,0}^{d_1,n} - \theta_{d_1} A_{b,1/2}^{d_1,n}, \quad k_{3c} = A_{b,0}^{d_2,n} - \theta_{d_2} A_{b,1/2}^{d_2,n}$$

continuity of pressure (14):

$$h_{12,13} = \frac{k_{4a}}{\sqrt{x_{10}}} - \frac{k_{4b,4c}}{\sqrt{x_{13,16}}} + k_{5a,5b}, \quad (\text{C.7})$$

$$h_{14,15} = \frac{k_{4a}}{\sqrt{x_{11}}} - \frac{k_{4b,4c}}{\sqrt{x_{14,17}}} + k_{5a,5b}, \quad (\text{C.8})$$

$$\begin{aligned} k_{4a} &= \left(f_M^p \sqrt{A_{b,M}^p} \right), \\ k_{4b} &= \left(f_0^{d_1} \sqrt{A_{b,0}^{d_1}} \right), \quad k_{4c} = \left(f_0^{d_2} \sqrt{A_{b,0}^{d_2}} \right), \\ k_{5a} &= -f_M^p + f_0^{d_1}, \quad k_{5b} = -f_M^p + f_0^{d_2}, \end{aligned}$$

654 and advancement of Q_b in time (16):

$$\begin{aligned} h_{16} &= k_{6a} - x_1 - \theta_p \left(\frac{x_3^2}{x_{12}} + B_{M+1/2}(x_{12}) \right) + \\ &\quad \gamma \left(F_{M+1/2}(x_3, x_{12}) + \frac{dB_{M+1/2}}{dx}(x_{12}) \right) \\ &= k_{6a} - x_1 + G_1(x_3, x_{12}), \end{aligned} \quad (\text{C.9})$$

$$\begin{aligned} h_{17,18} &= k_{6b,6c} - x_{4,7} + \theta_{d_1,d_2} \left(\frac{x_{6,9}^2}{x_{15,18}} + B_{-1/2}(x_{15,18}) \right) + \\ &\quad \gamma(F_{-1/2}(x_{6,9}, x_{15,18}) + \frac{dB_{-1/2}}{dx}(x_{15,18})) \\ &= k_{6b,6c} - x_{4,7} + G_{2,3}(x_{6,9}, x_{15,18}), \end{aligned} \quad (\text{C.10})$$

$$\begin{aligned} k_{6a} &= Q_{b,M}^{p,n} + \theta_p \mathcal{T}_{2,M-1/2}^{p,n+1/2} + \gamma \mathcal{S}_{2,M-1/2}^{p,n+1/2}, \\ k_{6b} &= Q_{b,0}^{d_1,n} - \theta_{d_1} \mathcal{T}_{2,1/2}^{d_1,n+1/2} + \gamma \mathcal{T}_{2,1/2}^{d_1,n+1/2}, \\ k_{6c} &= Q_{b,0}^{d_2,n} - \theta_{d_2} \mathcal{T}_{2,1/2}^{d_2,n+1/2} + \gamma \mathcal{T}_{2,1/2}^{d_2,n+1/2}. \end{aligned}$$

655 Equations (C.1)-(C.10) form a system of 18 non-linear equations, for 18 vari-
656 ables. However, we note that Equations (C.1)-(C.6) are linear in the vari-
657 ables. We can use this linearity to collapse the system significantly.

Given we are solving $h_i = 0$, (for $i = 1 \dots 18$), we first rearrange Equation

(C.3) for x_2, x_5 and x_8 , and substitute into Equation (C.2), to give (after rearrangement),

$$\begin{aligned} h_{a1} &= x_3 - x_6 - x_9 + k_7 = 0, \\ k_7 &= k_{1a} - k_{1b} - k_{1c}. \end{aligned} \quad (\text{C.11})$$

We then rearrange Equations (C.5) and (C.6) for x_{10}, x_{13} and x_{16} , and substitute into Equation (C.7), to give

$$h_{a2,a3} = \frac{k_{4a}}{\sqrt{k_{3a} - \theta_p x_3}} - \frac{k_{4b,4c}}{\sqrt{k_{3b,3c} + \theta_{d1,d2} x_{6,9}}} + k_{5a,5b} = 0. \quad (\text{C.12})$$

Equations (C.11) and (C.12) form a system of 3 non-linear equations with 3 unknowns. These can be solved for x_3, x_6 and x_9 using vector Newton method iterations, of the form

$$\mathbf{X}_a^{i+1} = \mathbf{X}_a^i - \mathcal{J}_a^{-1} \mathbf{H}_a(\mathbf{X}_a^i),$$

where $\mathbf{X}_a = (x_3, x_6, x_9)^T$ and $\mathbf{H}_a = (h_{a1}, h_{a2}, h_{a3})^T$. \mathcal{J}_a is the Jacobian matrix of \mathbf{H}_a and can be computed as

$$\mathcal{J}_a = \begin{bmatrix} 1 & -1 & -1 \\ \xi_1 & \xi_2 & 0 \\ \xi_1 & 0 & \xi_3 \end{bmatrix},$$

where

$$\begin{aligned} \xi_1 &= \frac{1}{2} k_{4a} \theta_p (k_{3a} - \theta_p x_3)^{-3/2}, \\ \xi_{2,3} &= \frac{1}{2} k_{4b,4c} \theta_{d1,d2} (k_{3b,3c} + \theta_{d1,d2} x_{6,9})^{-3/2}. \end{aligned}$$

Due to the small size of the system, the Jacobian inverse-product against \mathbf{H}_a can be calculated explicitly, though is only updated once each time step.

This system collapse allows us to efficiently solve for x_3, x_6 and x_9 . By substituting these values into Equations (C.3), (C.5) and (C.6) we can also easily calculate $x_2, x_5, x_8, x_{10}, x_{13}$, and x_{16} .

To solve for the remaining variables we first rearrange Equations (C.4)

671 for x_{11}, x_{14} , and x_{17} and substitute into Equations (C.8) to give

$$h_{b1,b2} = \frac{k_{4a}}{\sqrt{\frac{x_{12}}{2} + k_{2a}}} - \frac{k_{4b,4c}}{\sqrt{\frac{x_{15,18}}{2} + k_{2b,2c}}} + k_{5a,5b} = 0. \quad (\text{C.13})$$

We then rearrange Equations (C.9) and (C.10) for x_1, x_4 , and x_7 , and substitute into Equation (C.1) to give

$$\begin{aligned} h_{b3} &= k_8 + G_1(x_3, x_{12}) - G_2(x_6, x_{15}) - G_3(x_9, x_{18}) = 0 \\ k_8 &= k_{6a} - k_{6b} - k_{6c}. \end{aligned} \quad (\text{C.14})$$

672 Since we have already solved for x_3, x_6 , and x_9 , Equations (C.13) and (C.14)
 673 form a non-linear system with 3 unknowns. As with the first system, we solve
 674 these equations for x_{12}, x_{15} , and x_{18} using vector Newton method iterations
 675 of the form

$$\mathbf{X}_b^{i+1} = \mathbf{X}_b^i - \mathcal{J}_b^{-1} \mathbf{H}_b(\mathbf{X}_b^i),$$

676 where $\mathbf{X}_b = (x_{12}, x_{15}, x_{18})^T$, $\mathbf{H}_b = (h_{b1}, h_{b2}, h_{b3})^T$ and

$$\mathcal{J}_b = \begin{bmatrix} \xi_1 & \xi_2 & 0 \\ \xi_1 & 0 & \xi_3 \\ \xi_4 & \xi_5 & \xi_6 \end{bmatrix},$$

is the Jacobian of \mathbf{H}_b , with

$$\begin{aligned}
\xi_1 &= -\frac{1}{4} \left(\frac{x_{12}}{2} + k_{2a} \right)^{-3/2}, \\
\xi_{2,3} &= \frac{1}{4} \left(\frac{x_{15,18}}{2} + k_{2b,2c} \right)^{-3/2}, \\
\xi_4 &= \frac{\partial G_1}{\partial x_{12}}, \\
&= -\theta_p \left(-\left(\frac{x_3}{x_{12}} \right)^2 + \frac{1}{2} f R_{b,M+1/2}^0 \sqrt{A_{b,M+1/2}^0} x_{12}^{-3/2} \right) + \\
&\quad \gamma \left(\frac{2\pi R_{b,M+1/2}^0}{\delta} \frac{x_3}{x_{12}^2} - \frac{1}{2x_{12}} \frac{dB_{M+1/2}}{dx}(x_{12}) \right), \\
\xi_{5,6} &= -\frac{\partial G_{2,3}}{dx_{15,18}}, \\
&= -\theta_{d_1,d_2} \left(-\left(\frac{x_{6,9}}{x_{15,18}} \right)^2 + \frac{1}{2} f R_{b,-1/2}^0 \sqrt{A_{b,-1/2}^0} x_{15,18}^{-3/2} \right) + \\
&\quad \gamma \left(\frac{2\pi R_{b,-1/2}^0}{\delta} \frac{x_{6,9}}{x_{15,18}} - \frac{1}{2x_{15,18}} \frac{dB_{-1/2}}{dx}(x_{15,18}) \right).
\end{aligned}$$

As with the other 3×3 system, the size allows for efficient direct calculation of the Jacobian inverse-product against \mathbf{H}_b . Once a convergent solution (to within a desired tolerance) is reached, all remaining unsolved variables in \mathbf{X} can be solved through simple substitutions into the remaining equations of System (C.1)-(C.10).

Funding disclosures

BF is funded by the Rhodes Trust.

Creation of the virtual airway structures was performed prior to this study, and was funded partially through the EU FP 7 AirPROM project.

Figure 1 was created with the assistance of Ms Sanjana Sharma.

References

- [1] R. Bordas, C. Lefevre, B. Veeckmans, J. Pitt-Francis, C. Fetita, C. E. Brightling, D. Kay, S. Siddiqui, K. S. Burrowes, Development and anal-

- 690 ysis of patient-based complete conducting airways models, PLoS One
691 10 (12) (2015) e0144105.
- 692 [2] B. H. Foy, D. Kay, R. Bordas, Modelling responses of the inert-gas
693 washout and mri to bronchoconstriction, Respiratory Physiology & Neu-
694 robiology 235 (2017) 8–17.
- 695 [3] J. H. Mitchell, E. A. Hoffman, M. H. Tawhai, Relating indices of inert
696 gas washout to localised bronchoconstriction, Respiratory Physiology &
697 Neurobiology 183 (3) (2012) 224–233.
- 698 [4] A. Ben-Tal, Simplified models for gas exchange in the human lungs,
699 Journal of Theoretical Biology 238 (2) (2006) 474–495.
- 700 [5] C.-L. Lin, M. H. Tawhai, E. A. Hoffman, Multiscale image-based mod-
701 eling and simulation of gas flow and particle transport in the human
702 lungs, Wiley Interdisciplinary Reviews: Systems Biology and Medicine
703 5 (5) (2013) 643–655.
- 704 [6] K. Horsfield, F. G. Relea, G. Gunning, Diameter, length and branching
705 ratios in the bronchial tree, Respiration Physiology 26 (3) (1976) 351–
706 356.
- 707 [7] M. H. Tawhai, P. Hunter, J. Tschirren, J. Reinhardt, G. McLennan,
708 E. A. Hoffman, CT-based geometry analysis and finite element models
709 of the human and ovine bronchial tree, Journal of Applied Physiology
710 97 (6) (2004) 2310–2321.
- 711 [8] K. S. Burrowes, T. Doel, C. Brightling, Computational modeling of the
712 obstructive lung diseases asthma and copd, Journal of Translational
713 Medicine 12 (2) (2014) S5.
- 714 [9] M. H. Tawhai, K. S. Burrowes, Modelling pulmonary blood flow, Res-
715 piratory Physiology & Neurobiology 163 (1-3) (2008) 150–157.
- 716 [10] J. Tu, K. Inthavong, G. Ahmadi, Computational fluid and particle dy-
717 namics in the human respiratory system, Springer Science & Business
718 Media, 2012.
- 719 [11] M. S. Olufsen, C. S. Peskin, W. Y. Kim, E. M. Pedersen, A. Nadim,
720 J. Larsen, Numerical simulation and experimental validation of blood

- 721 flow in arteries with structured-tree outflow conditions, *Annals of*
722 *Biomedical Engineering* 28 (11) (2000) 1281–1299.
- 723 [12] N. Smith, A. Pullan, P. J. Hunter, An anatomically based model of
724 transient coronary blood flow in the heart, *SIAM Journal on Applied*
725 *Mathematics* 62 (3) (2002) 990–1018.
- 726 [13] R. W. Glenny, H. T. Robertson, Fractal modeling of pulmonary blood
727 flow heterogeneity, *Journal of Applied Physiology* 70 (3) (1991) 1024–
728 1030.
- 729 [14] G. S. Krenz, J. H. Linehan, C. A. Dawson, A fractal continuum model of
730 the pulmonary arterial tree, *Journal of Applied Physiology* 72 (6) (1992)
731 2225–2237.
- 732 [15] K. S. Burrowes, P. J. Hunter, M. H. Tawhai, Anatomically based fi-
733 nite element models of the human pulmonary arterial and venous trees
734 including supernumerary vessels, *Journal of Applied Physiology* 99 (2)
735 (2005) 731–738.
- 736 [16] W. Kang, M. H. Tawhai, A. R. Clark, R. C. Sá, E. T. Geier, G. K. Prisk,
737 K. S. Burrowes, In silico modeling of oxygen-enhanced mri of specific
738 ventilation, *Physiological reports* 6 (7) (2018) e13659.
- 739 [17] C. I. Fetita, F. Prêteux, C. Beigelman-Aubry, P. Grenier, Pulmonary
740 airways: 3-d reconstruction from multislice ct and clinical investigation,
741 *IEEE transactions on medical imaging* 23 (11) (2004) 1353–1364.
- 742 [18] K. Horsfield, Morphometry of the small pulmonary arteries in man.,
743 *Circulation Research* 42 (5) (1978) 593–597.
- 744 [19] B. H. Foy, D. Kay, A computational comparison of the multiple-breath
745 washout and forced oscillation technique as markers of bronchoconstric-
746 tion, *Respiratory physiology & neurobiology* 240 (2017) 61–69.
- 747 [20] B. H. Foy, S. Gonem, C. Brightling, S. Siddiqui, D. Kay, Modelling
748 the effect of gravity on inert-gas washout outputs, *Physiological reports*
749 6 (10) (2018) e13709.
- 750 [21] T. Pedley, R. Schroter, M. Sudlow, The prediction of pressure drop and
751 variation of resistance within the human bronchial airways, *Respiration*
752 *Physiology* 9 (3) (1970) 387–405.

- 753 [22] M. Paiva, Gas transport in the human lung, *Journal of Applied Physi-*
754 *ology* 35 (3) (1973) 401–410.
- 755 [23] B. Dutrieue, F. Vanholsbeeck, S. Verbanck, M. Paiva, A human acinar
756 structure for simulation of realistic alveolar plateau slopes, *Journal of*
757 *Applied Physiology* 89 (5) (2000) 1859–1867.
- 758 [24] M. S. Olufsen, Modeling the arterial system with reference to an aneste-
759 sia simulator, Ph.D. thesis, Roskilde Universitetscenter, Institut for
760 Studiet af Matematik og Fysik samt deres Funktioner i Undervisning,
761 Forskning og Anvendelser (1998).
- 762 [25] S. Sherwin, L. Formaggia, J. Peiro, V. Franke, Computational modelling
763 of 1d blood flow with variable mechanical properties and its application
764 to the simulation of wave propagation in the human arterial system,
765 *International Journal for Numerical Methods in Fluids* 43 (6-7) (2003)
766 673–700.
- 767 [26] K. Wesseling, J. Jansen, J. Settels, J. Schreuder, Computation of aortic
768 flow from pressure in humans using a nonlinear, three-element model,
769 *Journal of Applied Physiology* 74 (5) (1993) 2566–2573.
- 770 [27] T. R. Marrero, E. A. Mason, Gaseous diffusion coefficients, *Journal of*
771 *Physical and Chemical Reference Data* 1 (1) (1972) 3–118.
- 772 [28] K. S. Saladin, C. M. Porth, *Anatomy & physiology*, McGraw-Hill, 1998.
- 773 [29] R. Sander, Compilation of henry’s law constants (version 4.0) for water
774 as solvent., *Atmospheric Chemistry & Physics* 15 (8).
- 775 [30] A. M. Katz, *Physiology of the Heart*, Lippincott Williams & Wilkins,
776 2010.
- 777 [31] N. Pozin, S. Montesantos, I. Katz, M. Pichelin, I. Vignon-Clementel,
778 C. Grandmont, A tree-parenchyma coupled model for lung ventilation
779 simulation, *International journal for numerical methods in biomedical*
780 *engineering* 33 (11) (2017) e2873.
- 781 [32] A. D. Bordones, M. Leroux, V. O. Kheyfets, Y.-A. Wu, C.-Y. Chen,
782 E. A. Finol, Computational fluid dynamics modeling of the human pul-
783 monary arteries with experimental validation, *Annals of biomedical en-*
784 *gineering* (2018) 1–16.

- 785 [33] L. Grinberg, E. Cheever, T. Anor, J. R. Madsen, G. Karniadakis, Mod-
786 eling blood flow circulation in intracranial arterial networks: a compar-
787 ative 3d/1d simulation study, *Annals of biomedical engineering* 39 (1)
788 (2011) 297–309.
- 789 [34] E. Boileau, P. Nithiarasu, P. J. Blanco, L. O. Müller, F. E. Fossan,
790 L. R. Hellevik, W. P. Donders, W. Huberts, M. Willemet, J. Alastruey,
791 A benchmark study of numerical schemes for one-dimensional arterial
792 blood flow modelling, *International journal for numerical methods in*
793 *biomedical engineering* 31 (10) (2015) e02732.
- 794 [35] R. P. Mayo, J. Olsthoorn, D. S. Charnock-Jones, G. J. Burton, M. L.
795 Oyen, Computational modeling of the structure-function relationship in
796 human placental terminal villi, *Journal of biomechanics* 49 (16) (2016)
797 3780–3787.
- 798 [36] L. Gagnon, A. F. Smith, D. A. Boas, A. Devor, T. W. Secomb,
799 S. Sakadžić, Modeling of cerebral oxygen transport based on in vivo mi-
800 croscopic imaging of microvascular network structure, blood flow, and
801 oxygenation, *Frontiers in computational neuroscience* 10 (2016) 82.
- 802 [37] P. D. Robinson, P. Latzin, S. Verbanck, G. L. Hall, A. Horsley,
803 M. Gappa, C. Thamrin, H. G. Arets, P. Aurora, S. I. Fuchs, et al., Con-
804 sensus statement for inert gas washout measurement using multiple-and
805 single-breath tests, *European Respiratory Journal* 41 (3) (2013) 507–
806 522.
- 807 [38] L. Kent, P. Reix, J. Innes, S. Zielen, M. Le Bourgeois, C. Braggion,
808 S. Lever, H. Arets, K. Brownlee, J. Bradley, et al., Lung clearance index:
809 evidence for use in clinical trials in cystic fibrosis, *Journal of Cystic*
810 *Fibrosis* 13 (2) (2014) 123–138.
- 811 [39] R. Jensen, S. Stanojevic, K. Gibney, J. G. Salazar, P. Gustafsson,
812 P. Subbarao, F. Ratjen, Multiple breath nitrogen washout: a feasible
813 alternative to mass spectrometry, *PloS one* 8 (2) (2013) e56868.
- 814 [40] S. Verbanck, D. Schuermans, A. Van Muylem, M. Paiva, M. Nop-
815 pen, W. Vincken, Ventilation distribution during histamine provocation,
816 *Journal of applied physiology* 83 (6) (1997) 1907–1916.

- 817 [41] H. D. Litzlbauer, K. Korbel, T. L. Kline, S. M. Jorgensen, D. R. Eaker,
818 R. M. Bohle, E. L. Ritman, A. C. Langheinrich, Synchrotron-based
819 micro-CT imaging of the human lung acinus, *The Anatomical Record*
820 293 (9) (2010) 1607–1614.
- 821 [42] L. Formaggia, J.-F. Gerbeau, F. Nobile, A. Quarteroni, On the coupling
822 of 3D and 1D Navier–Stokes equations for flow problems in compli-
823 ant vessels, *Computer Methods in Applied Mechanics and Engineering*
824 191 (6-7) (2001) 561–582.
- 825 [43] B. Mauroy, M. Filoche, E. Weibel, B. Sapoval, An optimal bronchial
826 tree may be dangerous, *Nature* 427 (6975) (2004) 633.
- 827 [44] E. R. Weibel, *Geometry and dimensions of airways of conductive and*
828 *transitory zones*, Springer, 1963.